Complexity in the 3D stress fields of mid-ocean ridge tectonics: a manifestation of sub-crustal mush dynamics

Joyjeet Sen, Shamik Sarkar, Nibir Mandal*
Department of Geological Sciences, Jadavpur University
Kolkata 700032, India

Abstract

Mid-ocean ridge (MOR) systems evolve in strongly heterogeneous stress environments. However, the origin of such stress complexity still awaits a comprehensive explanation, which is the central theme of the present article. This study develops a thermo-mechanical model to demonstrate the multi-ordered 3D convective circulations, produced by decompression melting in the mushy region, as the key factor to modulate the MOR dynamics. The model mechanically couples the sub-ridge mushy regions with the elastic crustal layer within a mathematical framework of fluid-structure interaction (FSI) mechanics. FSI model simulations show that the heterogeneous stress field of a MOR forms characteristic segmented patterns on a time scale of million years, resembling axial as well as off-axis topographic morphologies observed in MORs. This article provides a model calculated estimate of the total stress tensor, focusing on the following components: across- and along-axis horizontal tension / compression ($\sigma^{\perp}$ and $\sigma^{\parallel}$) and across-axis horizontal shear stress ($\sigma^{\#}$) that dominantly control the ridge-axis morphologies. The stress mapping reveals a distinct 30 km wide axial zone of tensile $\sigma^{\perp}$ localization (median < 250 MPa), whereas compressive $\sigma^{\perp}$ localization (median < 100 MPa) in off-axis ridge-parallel linear belts on either side of the MOR axis. This finding leads to an alternative explanation for the off-axis ridge-parallel second-order hill topography, located at a distance of 20 km to 50 km, as a consequence of compressional $\sigma^{\perp}$ localization. Along-axis compressional $\sigma^{\parallel}$ concentrates in a row of ridge-normal narrow, 10 to 30 km wide stripes, giving rise to segmentation of the stress field on a wavelength of 40-150 km, which conforms to the second-order magmatic segmentation patterns of MORs. From $\sigma^{\#}$ mapping, it is also shown that ridge-transverse discontinuities, including transform offsets and transpression zones originate spontaneously from the FSI interactions during the MOR evolution.

Keywords: MOR stress fields, convective upwelling, mush complexes, fluid-structure interaction, magmatic segmentation, abyssal hills

*Corresponding author: nibirmandal@yahoo.co.in ; nibir.mandal@jadavpuruniversity.in;

1. Introduction

Mid-ocean ridges (MORs) are the most spectacular surface manifestations of the present-day divergent plate motion, dominated by ridge-axis normal tensile stresses. However, a range of morphological features, such as surface topography, transform faults and along-axis tectonic variations indicate that the stress fields are far more complex than a simple uniaxial tensional setting. Several studies have shown across-axis tension coupled with synchronously acting along-axis tension, implying that MORs can evolve in a bi-axial stress regime. A range of tectonic models, such as bi-axial global extension (Gudmundsson, 1995), flexural stresses resulting from spreading direction changes (Pockalny et al., 1996), stresses from isostatic compensation of the long-wavelength topography (Neves et al., 2004), and thermal stresses due to slab cooling (Choi et al., 2008; Sandwell, 1986), have been proposed to explain the origin of such bi-axial stress fields. A parallel line of works, in contrast, report along-axis compressional stress regimes. For example, Maia et al., 2016 have shown from earthquake focal mechanism solutions that the St Peter and St Paul islets, which represent parts of a major, 200 km long and 30 km wide submarine shear zone accommodate transpressive stresses along the northern transform fault of the St Paul system17, resulting in deep-crustal exhumation in this ridge segment. Similar ridge-parallel compressional stress regimes were reported earlier from the East Indian Ridge (Craddock et al., 2004). MORs often develop more complex heterogeneous stress fields, characterized by a close spatial association of along-axis compression and tension regimes (Parnell-Turner et al., 2017). All these observations suggest that MORs stresses can hardly be described by either an across-ridge uniaxial or a simple bi-axial tension model.

MOR systems generally sustain their stress activities away from the ridge axes, forming characteristic off-axis stress regimes, which are reported from geological and geophysical investigations like borehole breakout stress studies (Mildren and Hillis, 2000; Newmark et al., 1984). The most widely documented stress field is ridge-parallel off-axis

compressional fields, which are thought to originate from ridge-normal tension (Castillo et al., 1998; Newmark et al., 1984). Various mechanical models have been proposed to explain the origin of off-axis stress fields. For example, Parnell-Turner et al., (2017) developed a stress model based on the solutions of local micro-earthquakes originating from an active detachment at 13°20′N in the Mid-Atlantic Ridge. Their investigation recorded a remarkably high rate of seismic activity, with > 244,000 events detected along 25 km of the ridge axis and at depths of ~10 km below the seafloor, and recognized reverse-faulting events. Their stress model accounts for far-field horizontal forces (ridge-push or slab pull) at the plate extremities to explain the compressive stresses for reverse-faulting events within a global tensile regime. Intraplate earthquake focal mechanisms (Richardson et al., 1979; sites 92–94) also indicate a principal horizontal ENE-WSW trending compression zone within the Pacific plate. Similar off-axis compressional regimes are recorded from several other MORs (Moos and Zoback, 1990). In-situ borehole stress measurements near active spreading centers in the Ocean Drilling Program (ODP, Holes 504B and 765D, Newmark et al., 1984, DSDP Holes 504B and 395A, (Moos and Zoback, 1990) indicate that the maximum horizontal stress is compressive (>100 MPa), which is oriented normal to the spreading ridge axis.

The mechanical complexity of MORs is again manifested in their along-axis structural segmentation, often forming ridge transverse topographic morphologies (Macdonald et al., 1988). These transverse structures show stress intensification at the segment ends, which are explained in different ways, such as release of stress at the segment centres due to greater magmatic extension (Gràcia et al., 1999; Karson and Winters, 1992), variation in the properties of the elastic lithosphere (Behn and Ito, 2008; Dalton et al., 2014; Sibrant et al., 2018) and geometry of ridge-transform intersection (e.g., Morgan and Parmentier, 1984; Pollard and Aydin, 1984). Ridge-transverse structural segmentation is a reflection of across-axis shear stresses, further supported by strike-slip focal mechanisms. Step-like ridge geometry can

explain such shear stress fields. Ridge axes often undergo transcurrent movement, which is revealed from earthquake focal spread across them (Abercrombie and Ekström, 2001).

A direction of mechanical modelling deals with the mechanics of stress development in the divergent tectonics of MORs. Lithospheric flexural bending is perhaps the most widely accepted model, but used to explain the origin of ridge normal uniaxial tension that gives rise to ridge parallel normal faulting. Sohn and Sims, 2005 described plate bending as another possible mechanism for stress generation at MORs. In their model, bending stress accumulates as the plate progressively moves off axis, leading to maximum magnitudes, reaching 1.8 Gpa as a tensile stress at upper part of the lithosphere and 4 Gpa as a compressive stress at its lower part. However, the failure stresses at 1 km deep oceanic crust are estimated around 100 – 200 Mpa (for E=200 Mpa, Moos and Zoback, 1990); the actual stresses can thus never attain such large values. Parnell-Turner et al., (2017) bending model also yields large compressive stresses in the footwall of detachment faults in the axial regions, which would initiate reverse-faulting before such high stress magnitudes were reached. However, the bending model does not account for either along-axis tension or compression, as discussed in the preceding paragraphs. Several authors have considered topographic relief as a factor to show the development of axial tension (Luttrell and Sandwell, 2012; Morgan and Parmentier, 1984). All these calculations attempt to explain individual stress fields, ridge normal or parallel tension. However, there is no unified model to combine all types of stress fields into a single dynamics. Such a model is still required to resolve the problem of synchronous shear stress development in the framework of a biaxial stress regime.

The present article aims to meet these gaps taking into account the dynamic effects of underlying mushy regions. A thermomechanical model is developed to describe the three-dimensional stress field of a MOR in the perspective of magmatic processes beneath the ridge that include partial melting at depths, followed by convective upwelling of melts in porous

layers and subsequent transfer of the melt-mantle dynamics to the overlying crust. This modelling approach attempts to quantify the axial stresses, and across-ridge shear stresses, and finally validates the model estimates in the light of the morphological characters of the MOR systems, such as segment, axial topography, abyssal hill, transform and other types of faults.

2. Numerical Modelling

2.1. Approach

We combine four fundamental physical processes to conceptualize a representative model of the complex mid-ocean ridge systems. These are: 1) decompression melting at 60-30 km depth, 2) convection at 30 km, extending up to the crustal depth, and 3) fluid-solid interaction at the crustal base (4-5 km depth), and 4) stress versus topographic correlations in the solid crust. Each of them is treated with a distinctive theoretical consideration. Based on these four phenomena, we choose a three-layer model architecture (Fig. 1a; details provided in Supplementary section S.1) for the stress-field simulations of MORs.

2.1. Decompression melting

Considering the basic premises of decompression melting (explained in Supplementary section S.1), the present modelling takes into account a set of boundary conditions as described in Table 1. The model consists of a horizontal layer subjected to thermal perturbations at the base of the prismatic control volume (Numerical Domain), covering a horizontal distance of 15 km on either side of the MOR axis (Fig. 1a). The model depth is fixed at 28 km from the seafloor, considering that it corresponds to the threshold depth at which decompression melting ceases. The thermal perturbations are randomized within a temperature bound between 500^{o}C to 1440^{o}C (Mandal et al., 2018; Sarkar et al., 2014; Sen et al., 2023) , subject to a condition that the number of thermal points with temperatures above the liquidus must not exceed a threshold limit (20% of the total thermal

points). This specific boundary condition is imposed to constrain the melt production in the model approximated to natural cases (discussed in Supplementary section S.1).

2.2. Convection

The convection process starts to operate in the model following the decompression melting event, producing a critical amount of melts in the system to form mushy (solid + melt) materials in sub-ridge regions. It is noteworthy that the occurrence of mushy zones in sub-ridge mantle has been extensively reported in the earlier literature (e.g., Baines et al., 2009; Singh et al., 1998; Sinton and Detrick, 1992). Melts in the mushy regions set in buoyancy-driven convective circulations beneath the MOR. A detailed description of the theoretical treatment of mushy flows is provided in Sarkar et al., 2014 and Mandal et al., 2018. Here we highlight the basic theoretical principles used in the modelling of melt dynamics.

Mushy convection associates synkinematic crystallization and solidification that play a crucial role in the melt transport processes beneath MORs. To tackle the melt dynamics, the present model accounts for three material states: solid, melt and mushy, which are theoretically defined by melt fraction (MF), expressed as a linear function of temperature that fluctuates between the liquidus and solidus and modulates the pure melt versus pure solid states of a mushy system (Mandal et al., 2018; Sen et al., 2023). The system enthalpy is mediated via latent heat content associated with the phase transition (solid to melt or vice-versa). The corresponding enthalpy factor is also expressed as a linear function of MF. The melt transport in mushy materials is modelled by combining Navier-Stokes (NS) flow and Darcy's porous flow equations, where increasing MF switches Darcy to NS flows. Several earlier studies have invoked this theoretical concept to model the mechanics of mushy flows (e.g., Ricard et al., 2009; Turner et al., 2015). For the present problem, we follow Patankar, 1980 numerical method of heat and fluid flow simulation, utilizing the continuity equation,

momentum equation and the energy equation in enthalpy form. Three source terms are introduced to these equations: a Darcy term and a buoyancy term in the momentum equation; and an enthalpy term in the energy equation (Brent et al., 1988; Voller and Prakash, 1987). After incorporating these source terms, the three governing equations: continuity, momentum and energy equations can be expressed respectively as:

$$\nabla . v = 0 \tag{1}$$

$$\rho \frac{\partial}{\partial t} v + \rho v . \nabla v = -\nabla p + \mu_{fd} \nabla^2 v + S_g + S_D \tag{2}$$

$$\frac{\partial}{\partial t} (\rho h) + \nabla . (\rho v h) = \nabla . (a \nabla h) - S_h, \tag{3}$$

where p, ρ and μ_{fd} denote pressure, density and viscosity of the fluid domain, respectively. T, h and a represent temperature, enthalpy, and thermal diffusivity ($a = k/\rho c$, k and c are the thermal conductivity and specific heat, respectively). The fluid velocity, v is chosen to vary linearly with the melt fraction ϕ. In this single-phase idealization, the domain viscosity μ_{fd} is chosen to vary with temperature in a power-law function (Sarkar et al., 2014; Yongshun Chen and Morgan, 1990). In the momentum equation (Eq. 2) the source term S_D regulates the dominance of Darcy (i.e.porous) flows, whereas S_g implements the buoyancy factor through Boussinesque approximation. In the energy equation (Eq. 3) the source term S_h acts as an enthalpy factor to incorporate the energy involved in the solid-melt phase transformation. The mathematical expressions of these source terms are,

$$S_D = -C \frac{(1-\phi)^2}{(\phi^3+\varepsilon)} v \tag{4}$$

$$S_g = \rho g \theta \Delta T \tag{5}$$

$$S_h = \frac{\partial \rho \Delta H}{\partial t} + \nabla . (\rho v \Delta H). \tag{6}$$

C and ε in Eq.4 are constants, whose values are taken as 1e5 and 0.001, (Sarkar et al., 2014). In Eq.5 ΔT represents temperature fluctuations with respect to the reference temperature, and θ is the co-efficient of thermal expansion. In Eq. 6, ΔH is the mean latent heat content.

2.3 Fluid Structure Interaction

Considering a dynamic interaction of the elastic crust with the underlying mushy mantle as the key factor to determine the stress field in a MOR setting, we conceptualize the two-layer mechanical system in a theoretical framework of fluid-structure interaction (FSI) mechanics. The FSI mechanics treat a typical problem allowing the solid structures to interact with fluid, ideally both solid and fluid layers mechanically influencing each other. To model such a solid-fluid interaction, the classical mechanics approach uses the equations of motion for the fluid and the solid structure in the same tensor notation, which on applying D'Alembert's principle (Belytschko, 1980; Fig. 1b) follow:

$$\rho v'_i - \sigma_{ij,j} + f_i = 0, \tag{7}$$

where f_i is the body force term, ρ is the density, v_i is the velocity, and $\sigma_{ij,j}$ is the stress tensor. The fluid part is assumed to be homogeneous, Newtonian, and incompressible (Badia et al., 2008). The Cauchy stress tensor is,

$$\tau_f(u,p) = -pI + 2\mu G(u), \tag{8}$$

where p is the pressure, μ is the dynamic viscosity, and,

$$G(u) = \frac{1}{2}(\nabla u + (\nabla u)^T), \tag{9}$$

is the strain rate tensor, where u represents the fluid velocity.

Using Robin transmission (a linear combination of Dirichlet and Neumann components), we obtain a modified set of equations for the structure,

$$\frac{\beta_s}{\Delta t} w^{(K+1)} + {\tau_s}^{(k+1)}.n_s = \frac{\beta_s}{\Delta t} w^{(n)} + \beta_s u^{(k+1)} - {\tau_f}^{(k+1)}.n_f \quad \text{on} \quad \Sigma, \tag{10}$$

where β_s has a suitable positive and bounded value that determines the contribution of the Dirichlet component in the Robin transmission (Badia et al., 2008) (details provided in Supplementary S.2). The bounded positive value of β_s is set at 0.025, which is held constant spatially and temporally in a single simulation run, as well as in all the simulations. We assessed

impact of the constants on the model calculations, and found that the model results were not strongly sensitive to their values. The FSI mechanism of 3D mid-oceanic ridge system is 9oundary9ly discussed in Sen et al., (2023). The sub-problem for the fluid domain was tackled using finite volume computational dynamics code Fluent (Ansys 2016), whereas that for the structural domain was solved with the help of a finite element code for solid mechanics, ABAQUS CAE (Abaqus 2016). This computational study implemented the FSI operations using an indigenous code based on FORTAN, linked through Abaqus user-subroutines. A detailed description of the computational procedures is given in Supplementary section S2.

2.4. Elastic crustal deformation

Several authors (e.g., Buck et al., 2005) modelled the crust as a brittle layer to show shear failures (faults) in response to its extension and buckling. In contrast, we consider a body matrix depicting a series of three-dimensional stress fields, which allow us to map an array of tensile and compressive stress concentration zones on the top surface as well as within the elastic crust. The crustal strength at the MOR system is a critical parameter, as pointed out by previous researchers in the stress modelling. Based on the available estimates from volcanic rock systems (Behn et al., 2002; Behn and Ito, 2008; Gudmundsson, 2003), we varied Young's modulus I of the crustal layer between 5 and100 Gpa, finally keeping the *E* values in the line of recent studies (Olive and Dublanchet, 2020), where *E* is chosen in the order of 10 Gpa for the overlying crust.

3. Results: Stress tensor calculations

The FSI model simulations were run to investigate MOR stress fields, emphasizing upon the following stress components: along-axis compression and tension, and across-axis horizontal shear stress. This investigation also aims to relate the topographic development with the heterogeneous stress fields. The boundary-mechanical model produces three-

dimensional convective melt flows in the middle layer, initially forming a series of along-axis spreading centres located at distances of ~ 10 km to ~ 40 km in the top layer. Their distributions maintain a first order periodicity with an average distance of ~ 25 km (Fig. 1). In places, they are closely spaced to form a cluster of 3 to 6 centres in a 100 km length. The spreading centres often do not strictly maintain collinear arrangement, but show appreciable lateral offsetting with a magnitude of 5 km to 21 km. These initial spreading centres eventually coalesce with one another to form six spreading centres in course of time, at distances of 46-112 km. This article excludes a description of the three-dimensional melt-upwelling geometry, which has been covered at length in previous studies (Mandal et al., 2018; Sarkar et al., 2014; Sen et al., 2023). Multiple spreading centres that characterize a MOR setting develop a strongly heterogeneous, three-dimensional stress field in the elastic crust. The model estimates reveal that the stresses generated in the crust is comparable to that derived from ocean floor topography or tectonic movements (Luttrell and Sandwell, 2012).

The following sub-sections describe normal and shear stress components using their 3D contour plots at simulation run times: 1, 3, 5, and 7 Myr (Figs. 2-4 and Supplementary Figs. S1-S3). The descriptions adopt the symbol conventions of Luttrell and Sandwell, 2012; $\sigma^{\perp}$ and $\sigma^{\parallel}$ denote the normal stress components (σ_{xx} and σ_{zz} in the model Cartesian frame) perpendicular and parallel to the ridge axis, respectively, and $\sigma^{\uparrow}$ denote the vertical normal stress component (σ_{yy} in the model Cartesian frame). $\sigma^{\#}$ is used to express the horizontal shear stress component acting on a vertical plane perpendicular to the ridge axis (σ_{xz} in the model Cartesian frame). From a time-series analysis of the model runs, we investigate temporal and spatial variations of $\sigma^{\perp}$ and $\sigma^{\parallel}$ (Fig. 2a and Fig. 3a), with an objective to show the evolution of characteristic segmented MOR stress fields. $\sigma^{\#}$ mapping allows us to study transversely segmented structures commonly observed in mid-ocean ridges (Figure 4a-4b). To examine vertical variations in the stress field, we calculate the stresses in the top 2 km thick crustal

layer and the whole thickness of crust, denoted by subscripts, *tc* and *wc*, e.g., $\sigma^{\perp}_{tc}$ and $\sigma^{\parallel}_{wc}$ in their descriptions . The MOR model domain is subdivided broadly into two regions: axial zone (covering 15 km horizontal extent on either side of the axis) and off-axis region. Their stress fields are denoted as σ_{ax} and σ_{ox}, respectively. The symbolic presentation of various stress parameters used in this article is summarized in Table 2.

3.1 Ridge-perpendicular and ridge-parallel compression and tension

Model MORs develop typically an across-axis tensile ($\sigma^{\perp}$) regime in the axial zone, which is characteristically heterogeneous, consisting of multiple (9 – 10) segments of large $\sigma^{\perp}$ concentrations. These stress segments observed on the model surface are separated from each other at distances of 20 to 60 km along the ridge axis (Fig. 2a), and they persist down to the crustal base, albeit with their reducing size in the course of MOR evolution. The tensile axial regime is flanked by off-axis compressive regimes on either side of the axis, grossly running parallel to the ridge axis at approximately 2 Myr of the model run (Fig. 2a). Along-axis stress $\sigma^{\parallel}$ mapping reveals intense tensile and compressive stress localization, preferentially in ridge-normal narrow linear zones (Fig. 3a). Tensile zones that localize higher stresses at the ridge axis grow in time, often coalescing with one another to form wide tensile regimes, separated by narrow, 10 to 30 km wide compressive zones. Their axial spacing varies between 40 km and 150 km with an average of >100 km, giving rise to a segmented structure of the MOR. The system initially develops several smaller segments, visibly marked by across-axis compressive zone of relatively shorter lengths (< 50 km) and closely spacing (20 – 40 km), which are asymmetrically distributed about the ridge axis. The tensile regimes in the top layer are stronger than those in the bottom crustal layer (Fig. 2a).

Using the time-series FSI model results we performed box-plot analyses to study the temporal variation of stress fields in a MOR setting. The plots (Fig. 2b) show that ridge-

perpendicular stresses at axial zones remain predominantly tensile (+ $\sigma^{\perp}_{ax}$), leaving the off-axis regions dominated by compressive stresses (-$\sigma^{\perp}_{ox}$). In the top crustal layer both tensile and compressional $\sigma^{\perp}_{ax}$ attain their respective peak values, + 231 Mpa and -111 Mpa at 1 Myr (Fig. 2b), which steeply drops to +116 Mpa and -36 Mpa, respectively within 2.5 Myr. The median value of +$\sigma^{\perp}_{ax}$ decreases to 78 Mpa at 7 Myr, whereas that of -$\sigma^{\perp}_{ax}$ remains almost steady at ~ -38 Mpa (Fig. 2b). The stress analysis for the whole crustal thickness reveals higher median peaks of tensile and compressional $\sigma^{\perp}_{ax}$ = +273 Mpa and -135 Mpa at 1 Myr, which drop sharply to +138 Mpa and -51 Mpa at 2.5 Myr, and then moderately to +84 Mpa and -47 Mpa at 7 Myr (Fig. 2b). The stress estimates indicate variations of the across-ridge median tensile and compressive stresses from the shallow to deep-crustal regions, but at unequal rates, as revealed from their contrasting ratios: $(\sigma^{\perp}_{ax})_{WL}/(\sigma^{\perp}_{ax})_{TL}$ = 1.18 at 1 Myr and 1.08 at 7 Myr for tensile stresses, and 1.22 and 1.24 for compressional stresses (Fig. 2b). The axial zones of a mature MOR develop depth-wise more uniformly ridge-perpendicular tensile stresses regime in the crust, but heterogeneous compressive stresses with the crustal depth.

The off-axis stress ($\sigma^{\perp}_{ox}$) fields (+/- 15 km to +/- 75 km from the ridge axis) differ significantly from those in the axial regions in the dominance of compressive stresses over tensile stresses, in addition to their much lower stress magnitudes without showing sharp peaks (Fig. 2b). Median compressional $\sigma^{\perp}_{ox}$ in the top layer defines a blunt peak with a magnitude of 63 Mpa at 4 Myr, decreasing to 60 Mpa at 5 Myr that becomes almost steady with continued model run time. The off-axis regions develop minor tensile peaks (~ 21 Mpa) at 6 Myr, remaining steady with time (Fig. 2b). The whole-crust $\sigma^{\perp}_{ox}$ fields show a median compressive stress of 81 Mpa at 5 Myr, slightly decreasing to 79 Mpa at 7 Myr, with lower median tensile stresses of 17 Mpa at 5 Ma, increasing to 20 Mpa at 7 Myr (Fig. 2b). The ratio of compressional $\sigma^{\perp}_{ox}$ between the crustal top and bottom layers is 1.28 at 5 Myr and 1.32 at

7 Myr, whereas the ratio in the tensile zones is 0.88 at 6 Myr and 0.93 at 7 Myr. Evolved mid-ocean ridges develop the highest whole-crust ridge-normal tensile stresses in their axial zones (+84 Mpa) and the highest compressive stresses (-79 Mpa) in the off-axis regions (Fig. 2b).

The FSI models develop ridge parallel compressive and tensile stresses ($\sigma^{\parallel}$) in the axial zones of MORs, but with unequal magnitudes. Tensile $\sigma^{\parallel}$ in the top crustal layer attains a median peak of 247 Mpa at 1 Myr, which is significantly higher than the compressional median peak (192 Mpa). With time both the median peaks drop to 109 Mpa and 91 Mpa, respectively at 2.5 Myr, and further to 89 Mpa and 61 Mpa, respectively at 7 Myr (Fig. 3b). The whole-crust stress estimates show their relatively lower differences, e.g., 256 Mpa and 228 Mpa at 1 Myr, dropping to 123 Mpa and 100 Mpa at 2.5 Myr, and further to 98 Mpa and 70 Mpa at 7 Myr (Fig. 3b). The model results suggest that an evolved (7 Myr) MOR always develops along-axis compressive stresses significantly higher than the corresponding tensile stresses, as evident from their median ratios, 1.6 and 1.5 in the top and the whole crustal layers, respectively. However, there are secondary bi-axial tensile regions with axis-parallel tensile stresses more than that across the axis with their median ratios, 1.14 and 1.17 in the top and the whole crustal layer, respectively at 7 Myr (Fig. 3b). Off-axis $\sigma^{\parallel}$ fields in the top crustal layer develops lower ridge parallel tension and compression, marked by median peak of 25 Mpa and 33 Mpa, respectively at 3 – 4 Myr (Fig. 3b). The whole-crust calculations yield a similar trend of tensile and compressional $\sigma^{\parallel}$ in the off-axis regions with their peak values, 25 Mpa and 37 Mpa, which gradually decrease to 17 Mpa and 34 Mpa, respectively at 7 Myr. To summarize, the off-axis regions of a mature MOR concentrate along-axis compressive stress more in the deep-crustal layer than that in the top crustal layer, reflected from their median ratio, 1.36 at 7 Myr (Fig. 3b). The vertical stress component is described separately in Supplementary section S.4 and in Fig. S.1.

3.2 Ridge-transverse shear stress fields

Horizontal shear stresses ($\sigma^{\#}$) on across-ridge vertical planes reverse their sense of shear periodically in the axial direction, forming alternate band structures of counterclockwise (sinistral) and clockcwise (dextral) shear concentrations. Both dextral and sinistral shear bands develop at an angle of around 45^{o} to the ridge axis (Fig. 4a and Fig.4b), appearing mostly in the axial regions at initial stages of the model run. They retain their band structures with time, but reorient themselves at angles varying from 30^{o} to 60^{o} to the ridge axis, which further widen this range to 20^{o} -70^{o}, especially in the off-axis regions (Fig. 4a-4b). Some of the shear bands transgress the ridge axis, keeping their lateral continuity on either side of the axis (Fig. 4a). The boundaries between sinistral and dextral shear domains (marked by light green contours) are orthogonal to the ridge axis, giving rise to kinematic segmentation, which resembles those produced by transform faulting in natural MOR settings. Time-series model results show that the dextral and sinistral shear-stress domains in a young, 1 Myr old MOR are strongly heterogeneous in their size distributions, which evolves with time to reduce the heterogeneity, forming large shear domains at the cost of small ones at 7 Myr (Fig. 4a).

Fig. 4c presents a boxplot analysis to demonstrate varying dextral and sinistral shear stress magnitudes in the axial and off-axis regions obtained from the model runs. The foregoing description denote the dextral and sinistral shear stress as positive and negative quantities, respectively. At the axial zone in the top crustal layer their medians describe peaks values: +147 Mpa and -140 Mpa at 1 Myr, which progressively reduce to stable values: + 62 Mpa and – 57 Mpa at 7 Myr (Fig. 4c). On the other hand, the off-axis regions show their lower peak values: +21 Mpa and -21 Mpa at 4 Myr, subsequently decreasing further to +17 Mpa and +16 Mpa at 7 Myr. A separate figure for vertical shear contours and boxplots is provided in supplementary Fig. S.2.

We calculated the von-Mises stress (σ^{vm}) in the upper crustal layer to show the cumulative contributions of thre- dimensional shear stresses to MOR segmentation. The σ^{vm} contours (Fig. S.3 and in Supplementary section S.5) in the axial region reveal a median with peaks at 500 – 700 Mpa, which gradually drops to stable values of around 230-250 Mpa at 7 Myr. The σ^{vm} medians in off-axis regions are much lower, lying in the range 80 – 125 Mpa. The von-Mises stresses concentrate preferentially in linear strips oriented orthogonal to the ridge-axis at 5-7 Myr. These strips can act as potential across-ridge fracture zones, forming ridge segment structures, and provide mechanically favoured locations for transform faulting in extreme conditions.

4. Discussions

4.1. MOR stresses: a comparative analysis of the model estimates

Despite a significant progress in MOR modelling, the stress fields in MOR tectonic settings and their determining factors remained less explored. It is noteworthy that quantifying ridge parallel and perpendicular stresses is critically important to explain the origin of their morphological features (Gudmundsson, 1995), e.g., rift faulting and transpression zones. The sources of such stresses are mostly linked to magmatic diking, plate spreading, or thermal factors (Choi et al., 2008). Luttrell and Sandwell, 2012, however, provided estimates for a long and a short wavelength stress field taking into account the topographic reliefs of MOR segments. From ridge topography and transform offsets, they calculated ridge perpendicular tensile stresses, the magnitudes of which range from 10 to 100 Mpa. Their estimates yield significantly lower ridge-parallel tensile stresses (a maximum of 20 Mpa). According to Luttrel and Sandwell's model, the MOR settings generally develop biaxial stress fields with tension in along- and across-axis directions. Using a 2D boundary element model of the regional dyke systems in Iceland, (Gudmundsson, 2003) provided an

estimate for a dyke-tip tensile stress in the order of 10^2 Mpa, mediated through overburden compressive stress exerted by multiple layers of crust with Young's Modulus in the range 5-100 Gpa. (Kühn and Dahm, 2004), on the other hand, predicted the deviatoric stress state in a MOR. Using a simple boundary element model their calculated deviatoric stress magnitudes vary on a wide range, 0.05 Mpa to 5.3 Gpa. Similarly, the visco-plastic 3D MOR model of Gerya (2014) yields deviatoric stresses in the range ~ 1 Mpa to 1 Gpa.

The present model estimates, as described in Section 3, also show that the axial averages of directional stresses at mid-ocean ridges lie in the order of hundreds of Mpa, where their maxima can go up to 1 – 2 Gpa, suggesting that MOR systems can develop significant stresses, which originate entirely from the sub-ridge mush dynamics. The axis perpendicular stress medians lie within ~270 Mpa and axis-parallel stress medians lie within ~250 Mpa in axial zones. In off-axis regions the axis-perpendicular stress median varies within a limit of ~80 Mpa, whereas the axis-parallel stress medians attain a maximum of ~50 Mpa. The model results comprehensively describe the full range of MOR stress fields, the derivation of which remained incomplete in other models, such as topographic, tectonic, and plate-bending induced stress models. As an example, the topographic stress model of Luttrell and Sandwell, 2012 evaluates exclusively along- and across-axis tensile/compressional stresses in the axial zones. The present model, on the other hand, provides estimates for across-ridge shear stresses that develop synchronously with the normal stresses.

4.2. Manifestation of 3D stress field in MOR morphology

4.2.1. Formation of ridge segments and segment boundaries

Based on their along-axis length, offset length and durability, MOR segmentation can categorized into the following four types. A) Transform fault segments (Segment Length (SL): 300-500 km; Offset Length (OL) : >30 km; Duration (Du) : >10 Myr) b) Second order

segments (SL : 20-100 km at SSR and 50-250 km at FSR; OL : 2-30 km; Du : 1-10 My) c) Third order segments (SL : 10-50 km, OL : 0.5-2 km; Du : 0.01-1 Myr) d) Fourth order segments (SL : ~10 km; OL : <1 km; Du : ~0.001 Myr) (Macdonald et al., 1988). The FSI-based stress model allows us to map such segment boundaries observed in natural MORs as ridge-perpendicular compressive stress concentration zones (Fig. 5a.i – 5a.ii). Narrow high-compressive stripes define the primary magmatic segments, covering an across-axis length of ~ 60 km. The segments occur in different orders, with their along-axis wavelengths ranging from 30 km to 150 km (Fig. 5a.i), which agree with the second-order segmentation of ridge morphology. The FSI model also produces short, narrow high-compressive stress zones transverse to the axis, giving rise to higher-order segmentation structures. These smaller segments can be compared with the third-order MOR segments. These secondary transverse segment boundaries die out away from the ridge axis, leaving a few large segments as the MOR matures with time (7 Myr) (Fig. 5a.i). Our model reveals that across-axis narrow tensile zones, flanked by compressive stress boundaries on both sides, can produce segmentation structures. Several studies reported slender off-axis strips of compressional stress concentration of ridge-parallel, as obtained from the present model.

Consider now natural MORs to compare their segmentation structures with our model observations to discuss the physical implications of the stress analysis. The southern part (66^{o} – 56^{o}S) of the intermediate to fast spreading Pacific-Antarctic ridge (PAR) (Ondréas et al., 2001) that displays an axial valley to flat topography with spreading rate ~ 54-56 mm/yr consists of three segments (SL = 70-80 km) and two rift – rift overlapping spreading centres (OSC) (Fig. 5b.i). Its middle part has varying topography, forming valley, flat and highs, and spreading rates increasing from 56 mm/yr to 66 mm/yr northward over an axial distance of 650 km. The Heirtzler transform fault (TF) divides this part into two zones, southern zone consisting of five segments (SL = 30-150 km), and northern zone consisting of relatively

small, but four prominent segments. The fast-spreading (68-74 mm/yr) northern part of the PAR, on the other hand, has an axial high of 1100 km length, segmented by three major transform faults (SL = 50-80 km, OL = 40-60 km) (Fig. 5b.i). The ridge also contains a number of primary magmatic segments. The transform and non-transform segment boundaries are manifested as gravity low lines (Ondréas et al., 2001) (Fig. 5b.i). The present model produces along-axis compression/tension zones, forming large and small stress segments with their along-axis dimensions of 10-30 km and 40-150 km, respectively in close association. The similarity of non-transform segmentation patterns between the model and nature suggest that complex sub-ridge mushy flows is a responsible factor for the segmentation process in a mid-ocean ridge system. For further validation of the model calculated stress fields, we compare the model findings with the segmentation patterns of MAR (7^oS – 12^oS) (Figure 5b.ii), which, in overall, represent a typical slow-spreading (~32 mm/yr) ridge (DeMets et al., 1994). This portion of MAR has four segments (length: 70 km to 100 km); the two central segments show rifted axial highs, flanked by typical valleys in the north and south segments (Bruguier et al., 2003). The segment boundaries are marked by little offsets, where the discontinuity between two central segments are arguably marked by an OSC (Bruguier et al. 2003). This model study suggests that convergent boundaries (CZ in Fig. 5a.ii) that define primary magmatic segment (PMS) boundaries, as discussed above develop in the zone where two neighbouring magmatic spreading cells meet each other to form the first-order segmentation by compressive stripes on a wavelength of 40-150 km (Fig. 5a.i). The finding also explains the smaller segments as a manifestation of small-scale convection cells beneath the ridge axis. Both PAR and MAR have many inactive or fossil ridges in association with new ridges (Bruguier et al., 2003; Ondréas et al., 2001). Such inactive states of the ridges result from paucity of partial melt supply to the shallow level. MOR segment boundaries are marked by narrow vertical tensile stress ($\sigma^{\uparrow,t}$) zones, which

originated from the meeting lines of upwelling in the adjoining cells. These plate boundaries are topographically low zones, appearing as fracture zones in the natural ridges (Fig. 5b.i). The topographic parity between the model and nature supports the magmatic mechanism for fracture zone formation in MORs, like PAR.

Orthogonal offsetting is a common segmentation mechanism in PAR and MAR, operating on multiple orders on wavelengths of around 50 km, 70 km and 100 km. It seems to be a consequence of the heterogeneous stress field that gives rise to significant across-axis horizontal shear stresses with spatially varying shear sense, forming segmented structures. The FSI model suggests that the shear stress field can act as a destabilizing factor during the MOR evolution, leading to segmented structures by lateral offsetting. It is hypothesized that OSCs form at the meeting zone of two adjoining topographic reliefs with a lateral offset, which are found in the evolved model ridge (7 Myr) (Fig. 5a.i-a.ii), marked by two topographic highs with a lateral offset of ~ 10 km (Fig. 5a.i). The morphology resembles those observed in northern PAR (Fig. 5b.i) and MAR (Fig. 5b.ii). The ridge-parallel stress patterns in the model show a very narrow transverse compressive zone, sandwiched between two tensile zones over the adjacent axial highs at OSC (Fig. 5a.i).

4.2.2. Formation of ridge-parallel hills

Understanding the underlying dynamics of off-axis seafloor morphologies has rejuvenated the MOR studies with extensive fresh ground data and theoretical modelling, which provide new insights into their origin. Despite large variations in the genetic models, they converge at least to a point that the topographic morphologies originate from extensional crustal tectonics. However, crustal extension due to normal faulting can account for not more than 20% of the axial spreading in slow spreading ridges, which is further lower in case of fast spreading ridges (Bicknell et al., 1987; Macdonald, 1977; Solomon et al., 1988). One of the prevailing thoughts invokes the possible role of thermal stresses, attributed to differential

cooling of the upper part of the oceanic crust to account for such shortcoming. A major problem adheres to this proposition as the calculated thermal stresses are too low to cause yielding in the elastic-plastic crust, forming ridge-parallel normal faults (Turcotte, 1974). Off-axis axis-parallel highs and reliefs often occur in association with fast as well as slow spreading ridges on a stretch of hundreds of kilometres parallel to the ridge (Goff, 1991), characterized by smooth surface topography, which rules out the possibility of normal faulting as a primary process of their formation. Some studies have proposed this type of second-order topography as a manifestation of the whole-crust deformations (Buck et al., 2005). Our model results suggest that across-axis compressional tectonics (Fig. 6) can play a dominant role in shaping the seafloor away from the ridge. Both magmatic compressive and tensile stress regimes are simultaneously active in the upper crust, where they originate from the tractions offered by the 3D viscous flow of sub-ridge mushy materials. The compressive regimes become strong in magnitude, almost twice that of the tensile stresses at off-axis locations (Fig. 6), and capable of forming positive topographic elevations on the seafloor by compressional deformation of the oceanic crust. To explore their dynamics, we use the ridge-normal compressive stress maps (Fig. 6a) derived from the model runs at an interval of 1 Myr. This time interval is chosen considering the time scale of magmatic pulses in the seafloor topographic evolution (Crowley et al., 2015). The model map produces a pattern that resembles axis-parallel abyssal hills.

To delineate axis-parallel hills in a given time step of 1 Myr, we set a threshold ridge-perpendicular compressive stress (1 Mpa), and then mapped the stress zones to show the hill patterns at an instant during the spreading of a ridge axis. These hills localize discretely as lenticular bodies with their long dimensions (10 to 80 km) parallel to the ridge axis. Most of them are narrow in width (1 to 10 km) (Fig. 6a). They drift away from the axis in course of the spreading process, leaving the space for hill growth in the next step. The process

eventually gives rise to a row of ridge parallel hills formed sequentially away from the axis (Fig. 6a). Individual hills in successive steps grow in length, forming a first-order ridge-parallel morphology in wavy fashion with wavelengths to vary between 25 and 200 km. In overall, the morphology has a maximum horizontal width (10 km), tapering to a width of 1 km on a ridge-parallel distance of 20 to 70 km. The locational variation of off-axis compressive stress regimes also indicates different characteristics of faults at central and distal parts of the segments as well as along-axis gradient in the stress field (Behn et al., 2002).

The off-axis compressional topography grows synchronously with the rugged axial topography by normal faulting in the tensile regime, as observed in the present model. To support this finding, we choose the EPR (6°-9° S) (Fig. 6b), a fast-spreading ridge as an example. The bathymetric map of the seafloor around the ridge clearly reveals a parallel ridge-parallel hills on either side of the axial zone over a stretch of 50 km. The stress map shows that the compression fronts consist of a row of isolated maximum compressive stress zones at different time intervals (1-7 Myr), which would act as potential locations of topographic peaks aligned with the ridge-parallel off-axis highs. Smooth topographic hills, reported from the MAR occur as isolated ridge-parallel hills with a strike length of 15 to 30 km and an elevation between 500 to 2000 meters. Several petrological studies have postulated exhumation of lower crusts onto the ocean floor at MORs as an alternative mechanism of ophiolite emplacements (Dilek and Furnes, 2011), commonly observed in subduction zones and other convergent plate boundaries. The present model supports that such thrusting is possible to occur at a distance of 20 km from a ridge axis, where the crust can develop enough compressive stresses required for its shear failure and thrusting. To summarize, MORs develop locally compressional tectonic regimes, entirely driven by the upwelling dynamics of mushy materials in sub-ridge regions.

4.2.3. Horizontal transpression and transtension

Transform and non-transform offsets are common types of structural discontinuities in MOR systems, which are generally linked to their shear stress fields in the crustal upper layer (Behn et al., 2002; Neves et al., 2004; Persaud et al., 2017; Pollard and Aydin, 1984). Some studies accounted for thermal stresses developed during cooling to explain the origin of orthogonal transform offsets (Choi et al., 2008). Mechanical shear stresses are also held responsible for offset generation, considering that shear strength is low in the spreading direction (Freund and Merzer, 1976; Oldenburg, 1975). Two parallel ridges can link-up with each other by a ridge transverse strike-slip fault along the direction of low across-axis shear strength of the oceanic crust (Maia et al., 2016). All these models/hypotheses, however, do not apply to orthogonal segmentation of single straight ridges, as observed in many MORS, e.g., Mid Atlantic ridge (Carbotte et al., 1991). Our present models find no consistent relation between the shear stress and across-axis segment boundaries. Furthermore, superimposition of the horizontal shear stress fields on those of along-axis tensile and compressive stresses does not yield any orthogonal segmentation pattern (Supplementary Fig. S.4). It is found that the vertical shear stresses develop preferentially within along-axis tensile segments, ruling out the possibility of vertical shear stresses in segment formation. This shear stress may be an indicator of the three-dimensional subcrustal mush dynamics at segment centres. We can thus argue that across-axis transtensional zones (i.e., tension + shear), as reported from various natural MORs can be found at segment centres.

We compare an MAR stress data map with the along-axis compression and cumulative shear derived von-Misses stress from the present study, with an objective to test the applicability of the FSI model (Fig. 7a). Across-axis failure zones in the MAR (Fig. 7b) form segmented structures which agree with the von-Mises stress localization pattern in the model. Also, two along-axis compressive zones observed in the MAR (red arrows in Fig 7b;

close to at $31^0$15' discordant zone; and close to 38^0; Fox et al., 1991). It is to note that these stress maps should be treated as qualitative, where the exact location can show departures by 20 to 40 km (Luttrell and Sandwell, 2012). One of the two along-axis compression zones defines the $31^0$15' discontinuity, which was recorded as a segment boundary during the survey on MAR in the 31 to $34^0$30' S sector (Carbotte et al., 1991; Grindlay et al., 1991; Kuo and Forsyth, 1988). This segment boundary has only ~8 km offset (Fig. 7b), oblique to both the ridge and transform trends (Fox et al. 1991). The segment boundary and other non-transform segment boundaries (for example, $32^0$30' S and $33^0$30' S) are of magmatic origin, and their small offsets (8 km to 30 km) are attributed to isolated magmatic segments (Carbotte et al., 1991). It is also noteworthy that both the secondary segment boundaries at $31^0$15' and close to 38^0 are associated with some shear stresses, apart from the fact that the large offset fracture zones are dominated by shear, as evident from the stress maps (Fig. 7b). The hypothesis of magmatic segmentation, validated by gravity analysis (Kuo and Forsyth, 1988), multibeam data (Grindlay et al., 1991), magnetic analysis (Carbotte et al., 1991), and earthquake focal mechanism solutions (Luttrell and Sandwell, 2012) support the present model interpretation of across-axis structures as a product of mushy convections.

Using earthquake data several earlier studies have predicted along-axis tensile as well as compressional stresses at transform segment boundaries (Parnell-Turner et al., 2017; Rundquist and Sobolev, 2002). Some investigations suggested the ridge topography as a potential factor for tensile stresses along the ridge trend, giving rise to a trans-tensional tectonic setting in transform fault zones (Lonsdale, 1994). Transpression at MOR is typically conceived along transform faults, where a shear is thought to result from the opposing motion of two ridge segments, linked by a transform fault (Maia et al., 2016). This plate model implies that the shear and the compression originate from a single kinematics determined by two ridges approaching each other due to the spreading. This transpression model is

applicable to a system with decreasing ridge offset, but not a setting with increasing offset. Most of the earlier works dealt with transtensional and transpressional zones in terms of tectonic movements. The present model provides a new insight, claiming that sub-ridge magmatic activities can set a transtensional kinematics in MORs.

5. Conclusions

The principal findings of this model study are concluded along the following points. 1) Multi-ordered convection of sub-ridge mushy materials, produced by decompression melting under random thermal perturbations is the key physical process to determine the dynamics of mid-ocean ridges. 2) The mechanical coupling of mushy convection with the elastic crust, treated as fluid-structure interaction, develops a spatially complex stress field in a mid-ocean ridge, forming characteristic segmented stress localization patterns. This interaction dynamics can produce simultaneously along- and across-axis horizontal compression/tension as well as across-axis shear stress. Their median magnitudes can range 17 Mpa to 100 Mpa at steady states (after 7 Myr), implying that the magmatic process can largely contribute to the ridge dynamics, in addition to plate spreading. The plate spreading, however, cannot account for along-axis compression and across-axis shear stress in MORs, which originate essentially from the interaction of underlying mush convection with the overlying elastic crust. 3) MORs evolve in their axial zones dominantly by strong ridge normal tension, coupled with off-axis ridge-normal compression belt on either side of the ridge axis, which can be equated with off-axis ridge-parallel hills commonly observed in natural settings. 4) Along-axis compressive stresses localize in a row of narrow stripes across the ridge axis, resulting in segmentation of the stress field on a wavelength of 40-150 km. The second-order morphological segmentation of MORs reported in literature conforms to this stress segmentation characteristics, suggesting their origin linked to the sub-ridge

upwelling processes. 5) The estimated median axial stress magnitudes at MOR are in the scale of a few hundreds of Mpa (< 250 Mpa), and off-axis stresses are less than the axial stresses (< 100 Mpa). The top crustal layer develops stresses of relatively lower magnitudes than the corresponding deeper crustal layer. Off-axis compression stresses attain their peak values with a phase lag of a million years or more after the peak attainment of tensile stresses.

Data Availability Statement

The relevant data for bathymetric analysis are found at http://www.geomapapp.org/.

Acknowledgment

We express no conflict of interest. No datasets were generated during the current study. The DST-SERB has supported this work through the J. C. Bose fellowship (SR/S2/JCB-36/2012) to NM. SS gratefully acknowledges DST-SERB for his post-doctoral fellowship. JS is supported by a senior research fellowship (SRF) from DST-INSPIRE (IF170697), India.

References

Abercrombie, R.E., Ekström, G., 2001. Earthquake slip on oceanic transform faults. Nature 410. https://doi.org/10.1038/35065064

Badia, S., Nobile, F., Vergara, C., 2008. Fluid-structure partitioned procedures based on Robin transmission conditions. J Comput Phys 227. https://doi.org/10.1016/j.jcp.2008.04.006

Baines, A.G., Cheadle, M.J., John, B.E., Grimes, C.B., Schwartz, J.J., Wooden, J.L., 2009. SHRIMP Pb/U zircon ages constrain gabbroic crustal accretion at Atlantis Bank on the ultraslow-spreading Southwest Indian Ridge. Earth Planet Sci Lett 287. https://doi.org/10.1016/j.epsl.2009.09.002

Behn, M.D., Ito, G., 2008. Magmatic and tectonic extension at mid-ocean ridges: 1. Controls on fault characteristics. Geochemistry, Geophysics, Geosystems 9. https://doi.org/10.1029/2008GC001965

Behn, M.D., Lin, J., Zuber, M.T., 2002. Mechanisms of normal fault development at mid-ocean ridges. J Geophys Res Solid Earth 107. https://doi.org/10.1029/2001jb000503

Belytschko, T., 1980. Fluid-structure interaction. Comput Struct 12. https://doi.org/10.1016/0045-7949(80)90121-2

Bicknell, J.D., Sempere, J.C., Macdonald, K.C., Fox, P.J., 1987. Tectonics of a fast spreading center: A Deep-Tow and sea beam survey on the East Pacific rise at 19°30′ S. Mar Geophys Res (Dordr) 9. https://doi.org/10.1007/BF00338249

Brent, A.D., Voller, V.R., Reid, K.J., 1988. Enthalpy-porosity technique for modeling convection-diffusion phase change: Application to the melting of a pure metal. Numerical Heat Transfer 13. https://doi.org/10.1080/10407788808913615

Bruguier, N.J., Minshull, T.A., Brozena, J.M., 2003. Morphology and tectonics of the Mid-Atlantic Ridge, 7°-12°S. J Geophys Res Solid Earth 108. https://doi.org/10.1029/2001jb001172

Buck, W.R., Lavier, L.L., Poliakov, A.N.B., 2005. Modes of faulting at mid-ocean ridges. Nature 434. https://doi.org/10.1038/nature03358

Carbotte, S., Welch, S.M., MacDonald, K.C., 1991. Spreading rates, rift propagation, and fracture zone offset histories during the past 5 my on the Mid-Atlantic Ridge; 25°-27°30′ S and 31°-34°30′ S. Mar Geophys Res (Dordr) 13. https://doi.org/10.1007/BF02428195

Castillo, P.R., Natland, J.H., Niu, Y., Lonsdale, P.F., 1998. Sr, Nd and Pb isotopic variation along the Pacific-Antarctic risecrest, 53-57°S: Implications for the composition and dynamics of the South Pacific upper mantle. Earth Planet Sci Lett 154. https://doi.org/10.1016/s0012-821x(97)00172-6

Choi, E. seo, Lavier, L., Gurnis, M., 2008. Thermomechanics of mid-ocean ridge segmentation. Physics of the Earth and Planetary Interiors 171. https://doi.org/10.1016/j.pepi.2008.08.010

Craddock, J.P., Farris, D.W., Roberson, A., 2004. Calcite-twinning constraints on stress-strain fields along the Mid-Atlantic Ridge, Iceland. Geology 32. https://doi.org/10.1130/G19905.1

Crowley, J.W., Katz, R.F., Huybers, P., Langmuir, C.H., Park, S.H., 2015. Glacial cycles drive variations in the production of oceanic crust. Science (1979) 347. https://doi.org/10.1126/science.1261508

Dalton, C.A., Langmuir, C.H., Gale, A., 2014. Geophysical and geochemical evidence for deep temperature variations beneath mid-ocean ridges. Science (1979) 344. https://doi.org/10.1126/science.1249466

DeMets, C., Gordon, R.G., Argus, D.F., Stein, S., 1994. Effect of recent revisions to the geomagnetic reversal time scale on estimates of current plate motions. Geophys Res Lett 21. https://doi.org/10.1029/94GL02118

Dilek, Y., Furnes, H., 2011. Ophiolite genesis and global tectonics: Geochemical and tectonic fingerprinting of ancient oceanic lithosphere. Bulletin of the Geological Society of America 123. https://doi.org/10.1130/B30446.1

Fox, P.J., Grindlay, N.R., MacDonald, K.C., 1991. The Mid-atlantic Ridge (31°S-34°30′S): Temporal and spatial variations of accretionary processes. Mar Geophys Res (Dordr) 13. https://doi.org/10.1007/BF02428193

Freund, R., Merzer, M., 1976. The formation of rift valleys and their zigzag fault patterns. Geol Mag 113. https://doi.org/10.1017/S0016756800041315

Goff, J.A., 1991. A global and regional stochastic analysis of near-ridge abyssal hill morphology. J Geophys Res 96. https://doi.org/10.1029/91jb02275

Gràcia, E., Bideau, D., Hekinian, R., Lagabrielle, Y., 1999. Detailed geological mapping of two contrasting second-order segments of the Mid-Atlantic Ridge between Oceanographer and Hayes fracture zones (33°30°N-35°N). J Geophys Res Solid Earth 104. https://doi.org/10.1029/1999jb900161

Grindlay, N.R., Fox, P.J., MacDonald, K.C., 1991. Second-order ridge axis discontinuities in the south Atlantic: Morphology, structure, and evolution. Mar Geophys Res (Dordr) 13. https://doi.org/10.1007/BF02428194

Gudmundsson, A., 2003. Surface stresses associated with arrested dykes in rift zones. Bull Volcanol 65. https://doi.org/10.1007/s00445-003-0289-7
Gudmundsson, A., 1995. Stress fields associated with oceanic transform faults. Earth Planet Sci Lett 136. https://doi.org/10.1016/0012-821X(95)00164-8
Karson, J.A., Winters, A.T., 1992. Along-axis variations in tectonic extension and accommodation zones in the MARK Area, Mid-Atlantic Ridge 23°N latitude. Geol Soc Spec Publ 60. https://doi.org/10.1144/GSL.SP.1992.060.01.06
Kühn, D., Dahm, T., 2004. Simulation of magma ascent by dykes in the mantle beneath mid-ocean ridges. J Geodyn 38. https://doi.org/10.1016/j.jog.2004.06.002
Kuo, B.Y., Forsyth, D.W., 1988. Gravity anomalies of the ridge-transform system in the South Atlantic between 31 and 34.5° S: Upwelling centers and variations in crustal thickness. Mar Geophys Res (Dordr) 10. https://doi.org/10.1007/BF00310065
Lonsdale, P., 1994. Geomorphology and structural segmentation of the crest of the southern (Pacific-Antarctic) East Pacific Rise. J Geophys Res 99. https://doi.org/10.1029/93JB02756
Luttrell, K., Sandwell, D., 2012. Constraints on 3-D stress in the crust from support of mid-ocean ridge topography. J Geophys Res Solid Earth 117. https://doi.org/10.1029/2011JB008765
Macdonald, K.C., 1977. Near-bottom magnetic anomalies, asymmetric spreading, oblique spreading, and tectonics of the Mid-Atlantic Ridge near lat 37°N. Bulletin of the Geological Society of America 88. https://doi.org/10.1130/0016-7606(1977)88<541:NMAASO>2.0.CO;2
Macdonald, K.C., Fox, P.J., Perram, L.J., Eisen, M.F., Haymon, R.M., Miller, S.P., Carbotte, S.M., Cormier, M.H., Shor, A.N., 1988. A new view of the mid-ocean ridge from the behaviour of ridge-axis discontinuities. Nature. https://doi.org/10.1038/335217a0
Maia, M., Sichel, S., Briais, A., Brunelli, D., Ligi, M., Ferreira, N., Campos, T., Mougel, B., Brehme, I., Hémond, C., Motoki, A., Moura, D., Scalabrin, C., Pessanha, I., Alves, E., Ayres, A., Oliveira, P., 2016. Extreme mantle uplift and exhumation along a transpressive transform fault. Nat Geosci 9. https://doi.org/10.1038/ngeo2759
Mandal, N., Sarkar, S., Baruah, A., Dutta, U., 2018. Production, pathways and budgets of melts in mid-ocean ridges: An enthalpy based thermo-mechanical model. Physics of the Earth and Planetary Interiors 277. https://doi.org/10.1016/j.pepi.2018.01.008
Mildren, S.D., Hillis, R.R., 2000. In situ stresses in the southern Bonaparte Basin, Australia: Implications for first- and second-order controls on stress orientation. Geophys Res Lett 27. https://doi.org/10.1029/2000GL011537
Moos, D., Zoback, M.D., 1990. Utilization of observations of well bore failure to constrain the orientation and magnitude of crustal stresses: application to continental, Deep Sea Drilling Project, and Ocean Drilling Program boreholes. J Geophys Res 95. https://doi.org/10.1029/JB095iB06p09305
Morgan, J.P., Parmentier, E.M., 1984. Lithospheric stress near a ridge-transform intersection. Geophys Res Lett 11. https://doi.org/10.1029/GL011i002p00113
Neves, M.C., Bott, M.H.P., Searle, R.C., 2004. Patterns of stress at midocean ridges and their offsets due to seafloor subsidence. Tectonophysics 386. https://doi.org/10.1016/j.tecto.2004.06.010
Newmark, R.L., Zoback, M.D., Anderson, R.N., 1984. Orientation of in situ stresses in the oceanic crust. Nature 311. https://doi.org/10.1038/311424a0
Oldenburg, D.W., 1975. A Physical Model for the Creation of the Lithosphere. Geophysical Journal of the Royal Astronomical Society 43. https://doi.org/10.1111/j.1365-246X.1975.tb00642.x

Olive, J.A., Dublanchet, P., 2020. Controls on the magmatic fraction of extension at mid-ocean ridges. Earth Planet Sci Lett 549. https://doi.org/10.1016/j.epsl.2020.116541
Ondréas, H., Aslanian, D., Géli, L., Olivet, J.L., Briais, A., 2001. Variations in axial morphology, segmentation, and seafloor roughness along the Pacific-Antarctic Ridge between 56°S and 66°S. J Geophys Res Solid Earth 106. https://doi.org/10.1029/2000jb900394
Parnell-Turner, R., Sohn, R.A., Peirce, C., Reston, T.J., MacLeod, C.J., Searle, R.C., Simão, N.M., 2017. Oceanic detachment faults generate compression in extension. Geology 45. https://doi.org/10.1130/G39232.1
Patankar, S. V., 1980. Numerical heat transfer and fluid flow. https://doi.org/10.13182/nse81-a20112
Persaud, P., Tan, E., Contreras, J., Lavier, L., 2017. A bottom-driven mechanism for distributed faulting in the Gulf of California rift. Tectonophysics 719–720. https://doi.org/10.1016/j.tecto.2016.11.024
Pockalny, R.A., Gente, P., Buck, R., 1996. Oceanic transverse ridges: A flexural response to fracture-zone-normal extension. Geology 24. https://doi.org/10.1130/0091-7613(1996)024<0071:OTRAFR>2.3.CO;2
Pollard, D.D., Aydin, A., 1984. PROPAGATION AND LINKAGE OF OCEANIC RIDGE SEGMENTS. J Geophys Res 89. https://doi.org/10.1029/JB089iB12p10017
Ricard, Y., Šrámek, O., Dubuffet, F., 2009. A multi-phase model of runaway core-mantle segregation in planetary embryos. Earth Planet Sci Lett 284. https://doi.org/10.1016/j.epsl.2009.04.021
Richardson, R.M., Solomon, S.C., Sleep, N.H., 1979. Tectonic stress in the plates. Reviews of Geophysics. https://doi.org/10.1029/RG017i005p00981
Rundquist, D. V., Sobolev, P.O., 2002. Seismicity of mid-oceanic ridges and its geodynamic implications: A review. Earth Sci Rev. https://doi.org/10.1016/S0012-8252(01)00086-1
Sandwell, D.T., 1986. Thermal stress and the spacings of transform faults. J Geophys Res 91. https://doi.org/10.1029/jb091ib06p06405
Sarkar, S., Baruah, A., Dutta, U., Mandal, N., 2014. Role of random thermal perturbations in the magmatic segmentation of mid-oceanic ridges: Insights from numerical simulations. Tectonophysics 636. https://doi.org/10.1016/j.tecto.2014.08.008
Sen, J., Sarkar, S., Mandal, N., 2023. Control of mush complex viscosity on mid-ocean ridge topography: A fluid–structure model analysis. Physics of Fluids 35. https://doi.org/10.1063/5.0152667
Sibrant, A.L.R., Mittelstaedt, E., Davaille, A., Pauchard, L., Aubertin, A., Auffray, L., Pidoux, R., 2018. Accretion mode of oceanic ridges governed by axial mechanical strength. Nat Geosci 11. https://doi.org/10.1038/s41561-018-0084-x
Singh, S.C., Kent, G.M., Collier, J.S., Harding, A.J., Orcutt, J.A., 1998. Melt to mush variations in crustal magma properties along the ridge crest at the southern East Pacific Rise. Nature 394. https://doi.org/10.1038/29740
Sinton, J.M., Detrick, R.S., 1992. Mid-ocean ridge magma chambers. J Geophys Res 97. https://doi.org/10.1029/91JB02508
Sohn, R.A., Sims, K.W.W., 2005. Bending as a mechanism for triggering off-axis volcanism on the East Pacific Rise. Geology 33. https://doi.org/10.1130/G21116.1
Solomon, S.C., Huang, P.Y., Meinke, L., 1988. The seismic moment budget of slowly spreading ridges. Nature 334. https://doi.org/10.1038/334058a0
Turcotte, D.L., 1974. Are transform faults thermal contraction cracks? J Geophys Res 79. https://doi.org/10.1029/jb079i017p02573

Turner, A.J., Katz, R.F., Behn, M.D., 2015. Grain-size dynamics beneath mid-ocean ridges: Implications for permeability and melt extraction. Geochemistry, Geophysics, Geosystems 16. https://doi.org/10.1002/2014GC005692

Voller, V.R., Prakash, C., 1987. A fixed grid numerical modelling methodology for convection-diffusion mushy region phase-change problems. Int J Heat Mass Transf 30. https://doi.org/10.1016/0017-9310(87)90317-6

Yongshun Chen, Morgan, W.J., 1990. A nonlinear rheology model for mid-ocean ridge axis topography. J Geophys Res 95. https://doi.org/10.1029/jb095ib11p17583

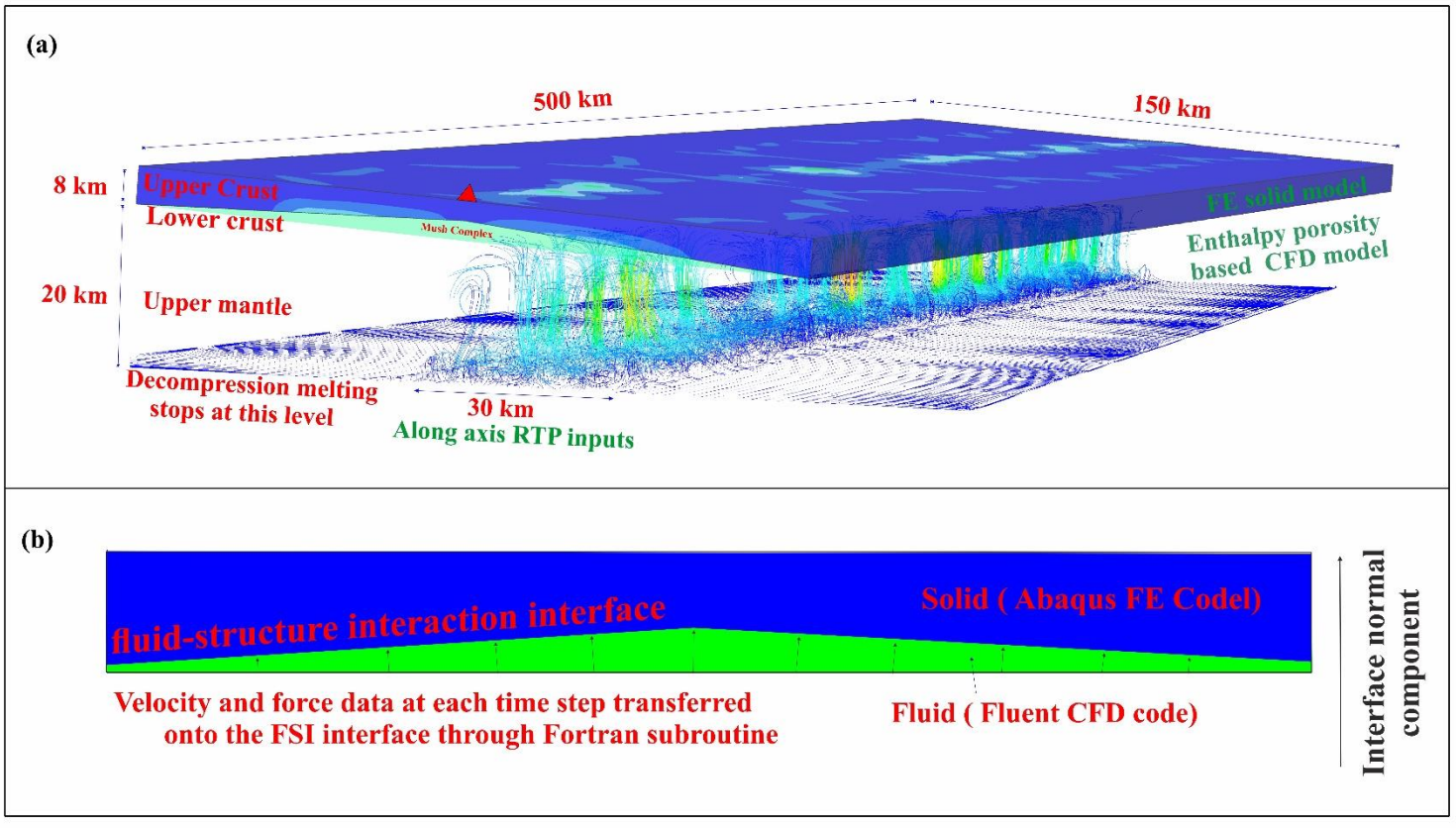

Figure 1

A schematic diagram of the MOR model, showing upper-mantle convective upwelling beneath the crust. a) A rectangular zone of melt 'points' that marks cessation of decompression melting and formation of random thermal perturbations (RTP), with a temperature fluctuation in the range 500 to 1400 ^{0}C (Sarkar et al., 2014). The RTP points act as initiation of convection in the shallower part of the mantle beneath the MOR, indicated by flow path lines. The lower crustal mush complex (MC) transfers motion and force to the crustal base, causing an elastic deformation in thin crust (Sen et al., 2023). b) Diagrammatic explanation of the Fluid Structure Interaction (FSI) in the two-layer MOR model.

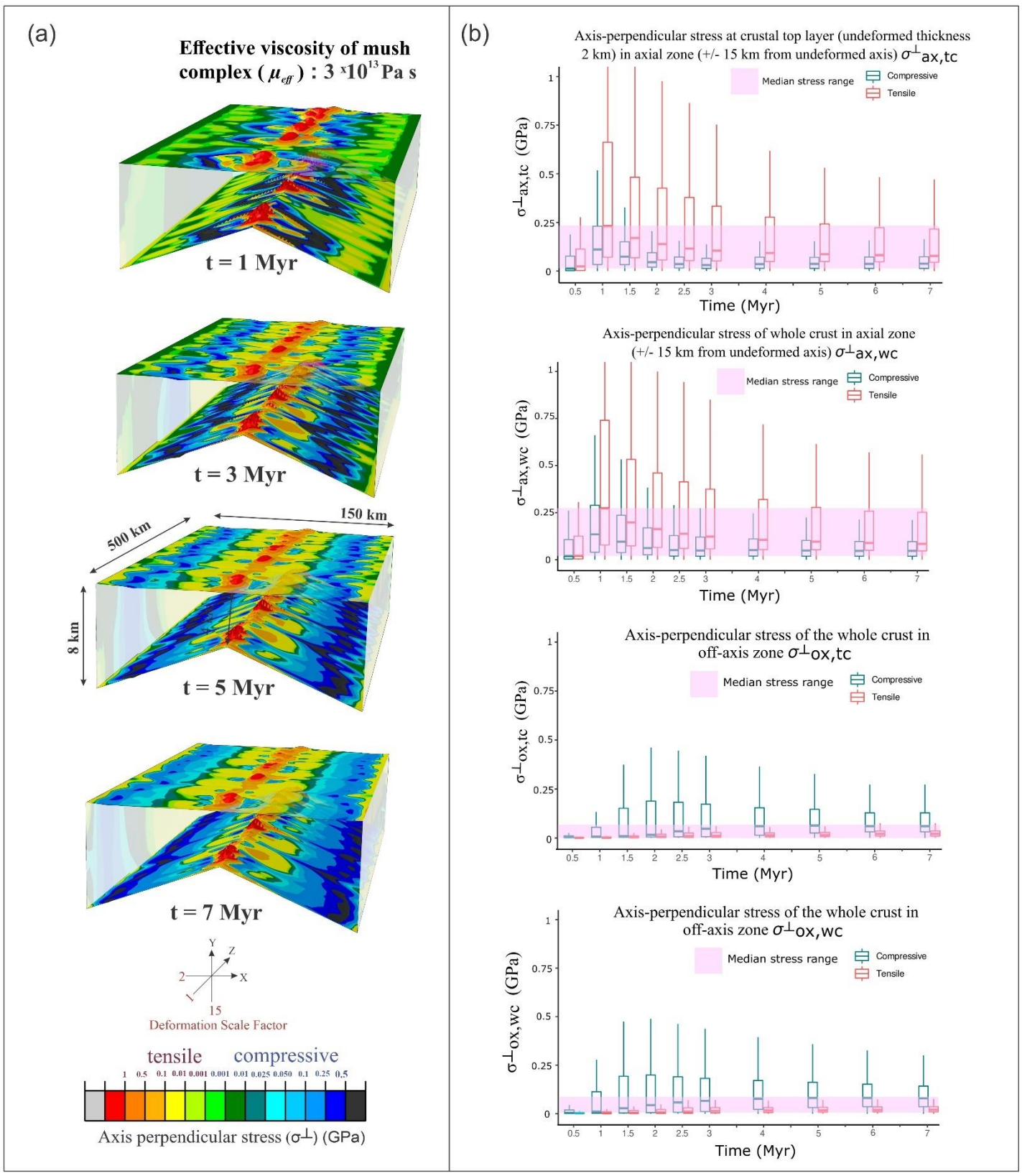

Figure 2

Time series 3D contour plots for ridge-perpendicular stress and their statistical box-plots. a) Ridge-perpendicular stress ($\sigma^{\perp}$) contours (σ_{xx} in Cartesian model settings) at 1, 3, 5, and 7 Myr (Spatial scales: vertical = 15, along-axis = 1, across-axis = 2). Transparent model views reveal the stress distributions in both top and bottom layers. b) Statistical box-plots of the stresses in different crustal domains (axial zone, off-axis zone, top-crustal layer, whole-crust) with their medians and quartiles.

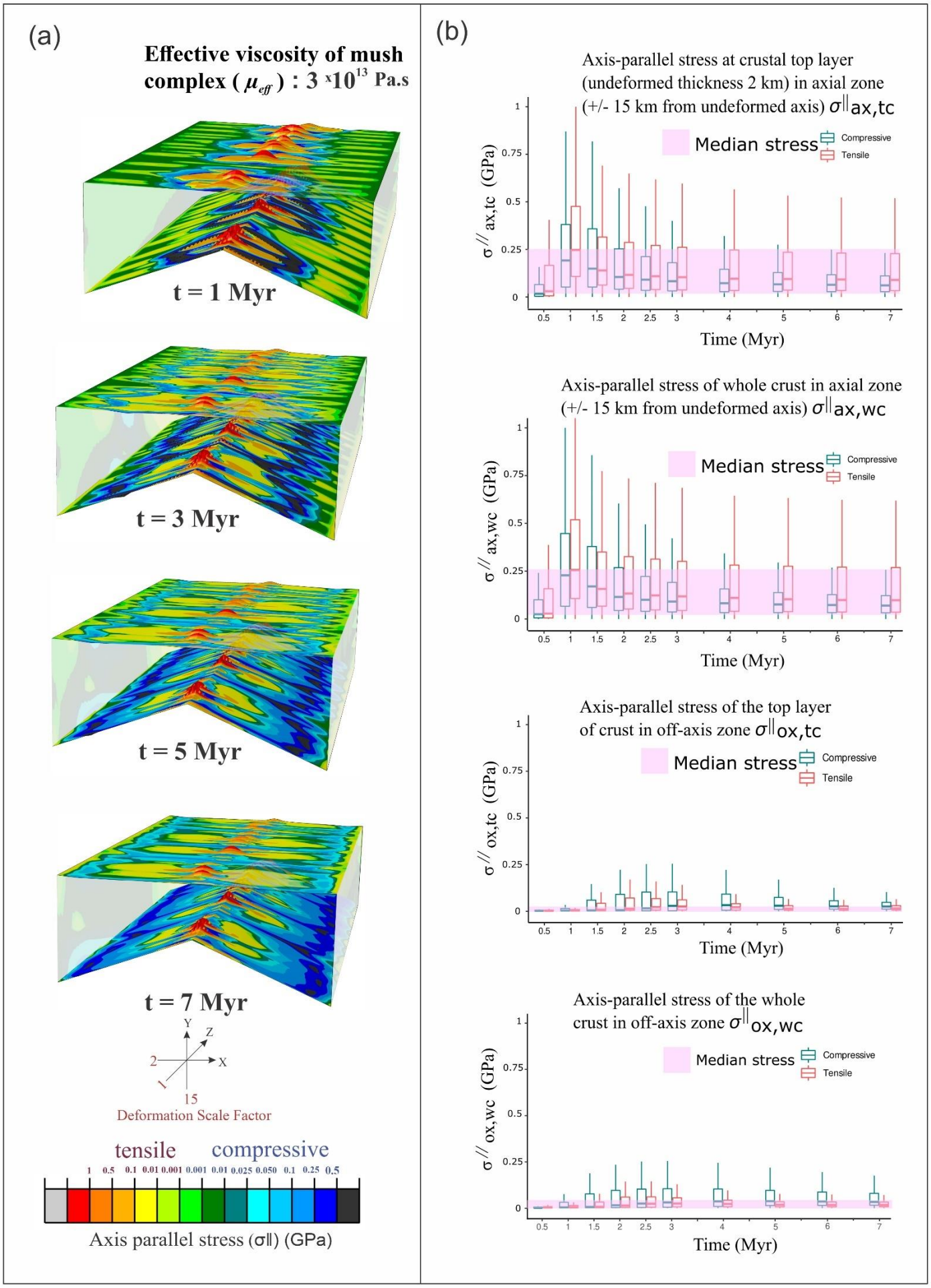

Figure 3

3D contour plots of ridge-parallel stress ($\sigma^{\|}$) fields and their statistical (box-plots) representations. a) Ridge-parallel stress ($\sigma^{\|}$)contours (σ_{zz} in Cartesian model frame) in model runs at 1, 3, 5, and 7 Myr. b) Their statistical box-plots with the stress medians and quartiles.

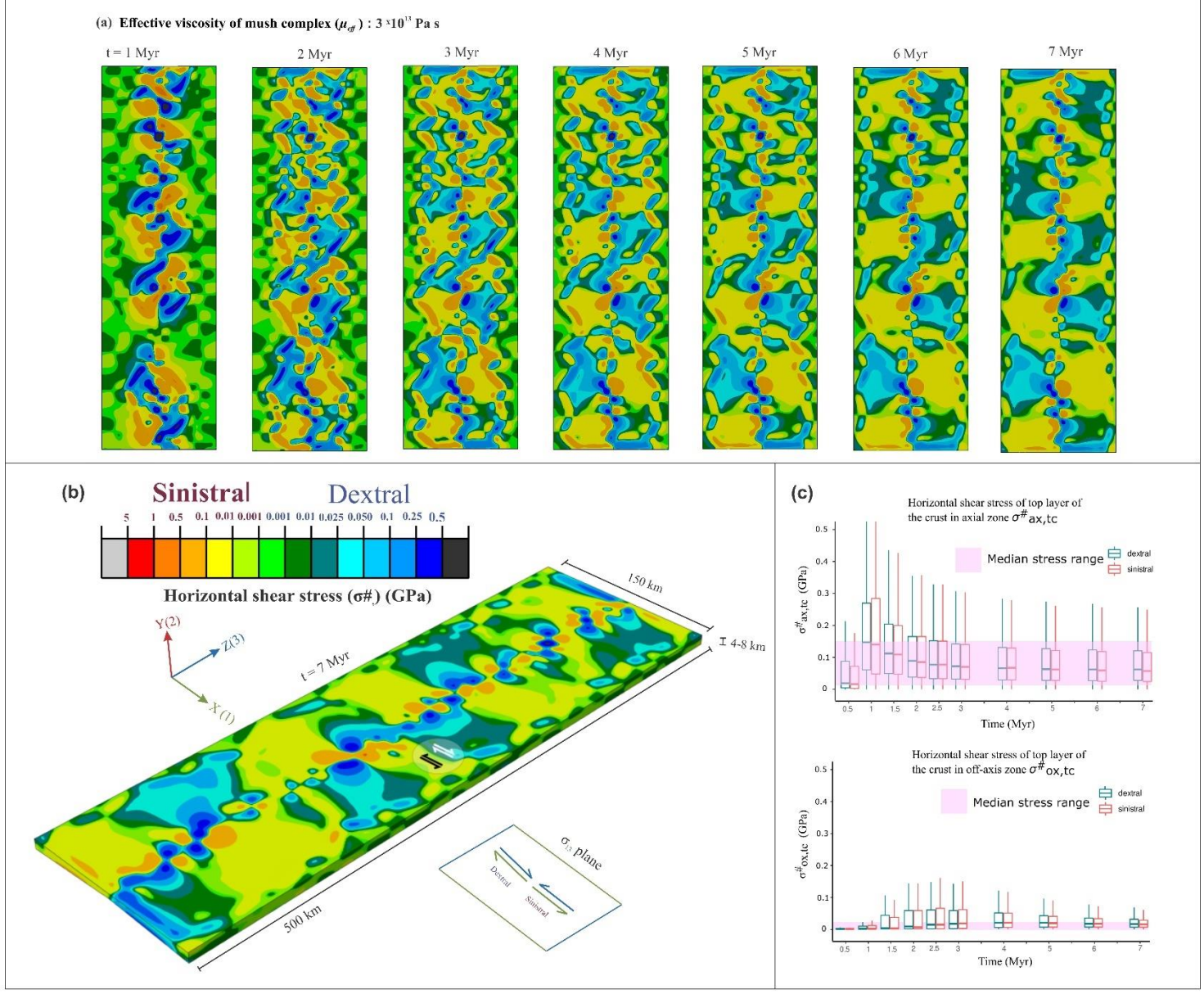

Figure 4

A series of contour plots showing horizontal shear stresses ($\sigma^{\#}$) in MOR and their corresponding box-plot presentation. a) Horizontal shear stress contours (σ_{xz} in Cartesian model settings) at 1, 2, 3, 4, 5, 6, and 7 Myr. Note counterclockwise (sinistral) and clockwise (dextral) stress patterns. b) Three-dimensional presentations of the sinistral and dextral horizontal shear. c) Statistical box-plots, showing the median values and their quartiles in the shear stress fields.

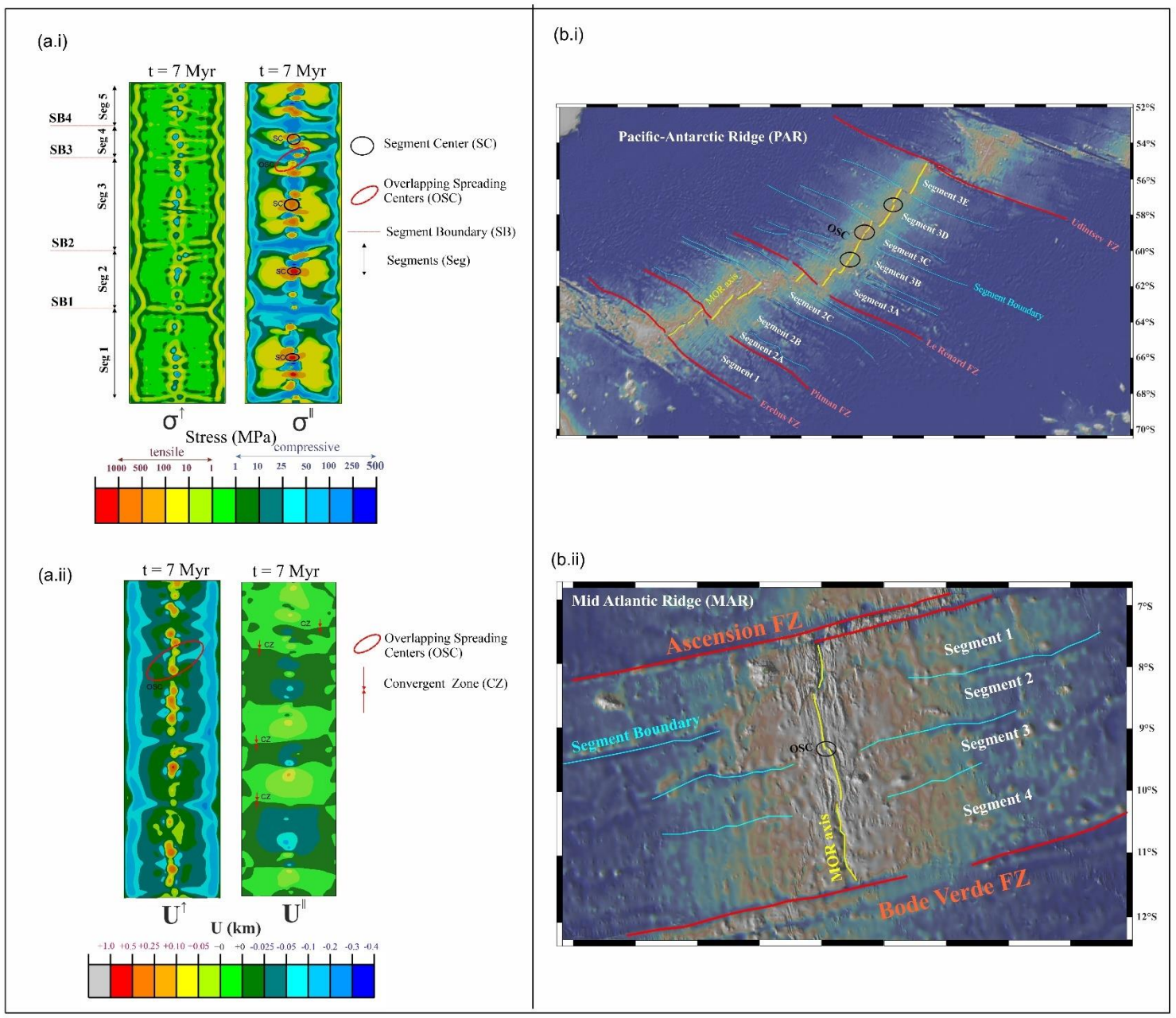

Figure 5

Contours of vertical stress ($\sigma^{\uparrow}$) and ridge-parallel stress ($\sigma^{\parallel}$) at 7 Myr (a.i), and contour plots of the vertical ($U^{\uparrow}$) and ridge-parallel displacements ($U^{\parallel}$) (a.ii), showing different mid oceanic ridge segmentation features, including segment centers, overlapping spreading centers, and segment boundaries. (b.i) Segments of the Pacific Atlantic Ridge and (b.ii) the Mid Atlantic Ridge, displaying morphological features similar to those inferred from the FSI model.

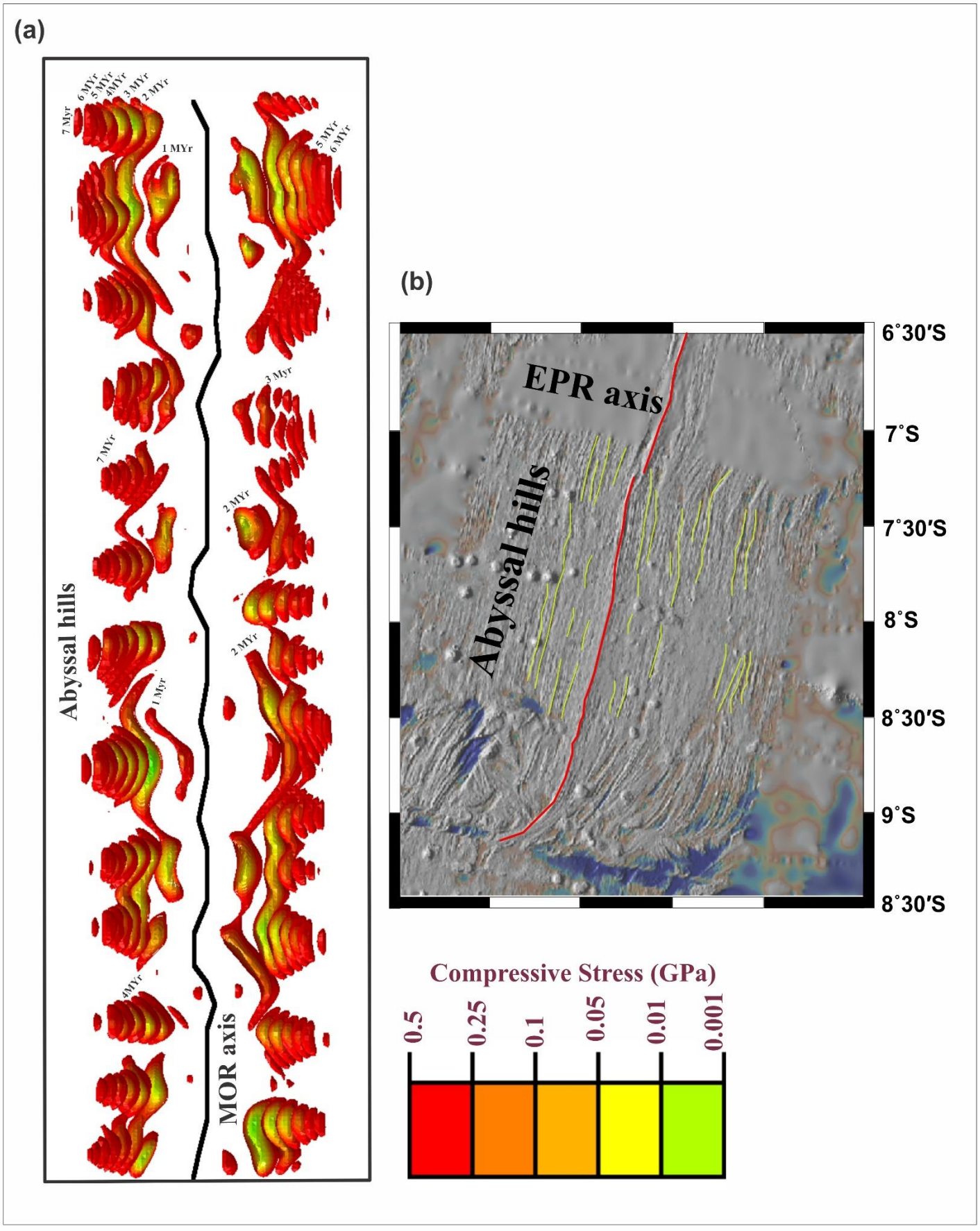

Figure 6

a) Across-axis compressive stress ($\sigma^{\perp,c}$) fields of a MOR obtained from the FSI model simulations. It is noteworthy that the model produces compression stress regimes in the form of ridge parallel stripes, which closely resemble ridge-parallel abyssal hill ranges. b) An EPR segment with systematically arranged ridge-parallel abyssal hills.

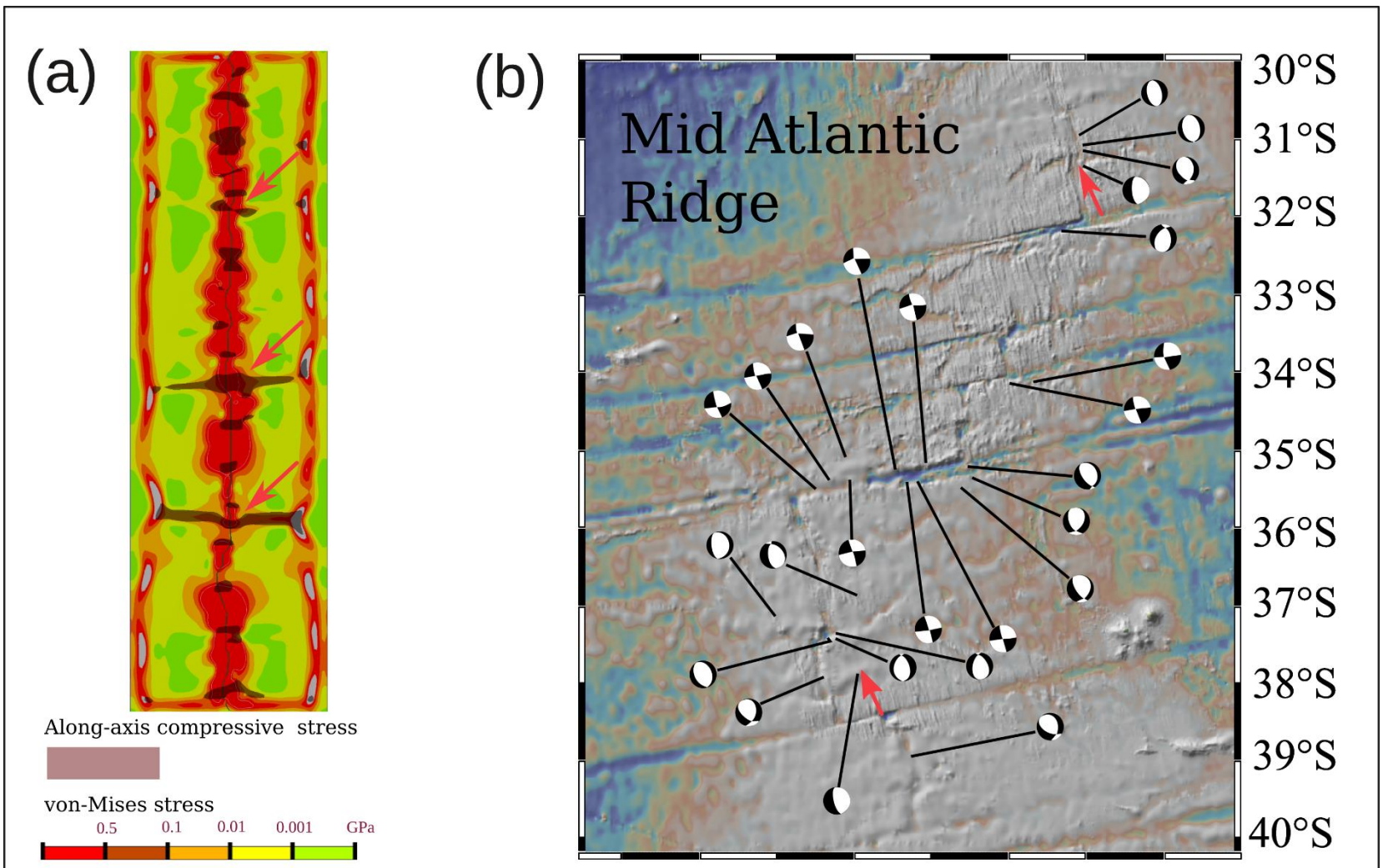

Figure 7

a) Calculated plots of the von-Misses stresses (σ^{vm}) and along-axis compressive stresses ($\sigma^{\|,c}$) . The von-misses stresses localize preferentially in an array of ridge normal bands, resulting in MOR segmentation (red arrow). b) A portion of the MOR showing two ridge segments (red arrow). Details are given in the manuscript, in section 4.2.3.

Supplementary materials

S.1 Model design

We implemented the FSI approach in a 3D finite element model, appropriately designed to represent the most typical structure of mid-ocean ridges (Fig. 1). This is a three-layer structure: 1) basal layer (decompression melting zone), 2) intermediate layer (convection zone) and 3) top layer, each of them characterized by specific ridge-forming processes. The basal layer, covering depths from 32 to 60 km, is set to simulate the decompression melting zone encompassing a horizontal distance of 50 km symmetrically on either side of the MOR axis. The intermediate layer is the most critical layer to mediate the mechanical coupling between the decompression melting zone and the top solid crustal layer. Based on the available data on sub-ridge mushy zones (Edmonds et al., 2019; Lissenberg et al., 2019; Singh et al., 1998, 2006; Sinton & Detrick, 1992; Sparks et al., 2019), the thickness of this layer is chosen as ~28 km. Its interface with the basal layer is subjected to random thermal perturbations (attributed to heterogeneous melt upwelling in the basal layer) in an along-axis narrow zone (Fig. 1), where the temperature fluctuates randomly between an upper (liquidus set at 1400^{o}C) and a lower (solidus set at 500^{o}C) bound. Melt-driven local scale convection processes that characterize this middle layer are modelled by combining Navier-Stokes and Darcy (porous) flow dynamics, as discussed in section 2.2. The convecting flows develop 3D structures, with a strong spatial heterogeneity along the ridge axis. The top layer represents the solid oceanic crust with a minimum thickness of 4 km at the MOR centre, increasing to a thickness of 8 km at the model edge. This layer is modelled as an isotropic elastic layer with all its elastic properties approximated to an average oceanic crust (Table 1). The key step in our FSI modelling concerns mechanical bridging

between the middle fluid and the top solid layers. To reveal the sole contribution of sub-ridge melt processes to the MOR stress fields, the present modelling excludes a pre-fixed weak zone for melt intrusion in the solid crust.

S.2 Decompression melting beneath MOR

The phenomenon of decompression melting beneath a MOR system can take place in a depth range of 60-30 km, provided a set of conditions is satisfied. The primary condition, as defined by (Mckenzie & Bickle, 1988) is that an isotherm below the mid-oceanic ridge must be deflected upward from its horizontal position. In addition, the mantle adiabats would ideally follow potential temperature lines up to the surface, maintaining an isentropic state, and would change their courses as soon as they meet the solidus when there is a departure from the isentropic state with the onset of melting. Mckenzie & Bickle, (1988) used a value of 250 J/kg/^{0}C and obtained a thermal change of 80 to160 ^{0}C in the isentropic based potential temperature and the actual temperature at the moment of decompression melting, depending on the variation of potential temperature in the mantle region (Mckenzie & Bickle, 1988).

Considering the MORB petrogenesis, the modelling of decompression melting demands a criticality analysis to constrain the melt fraction. Petrological calculations suggest a maximum of 24% melt for the polybaric fractional melting of lherzolite at the plagioclase-spinel lherzolite transition (Presnall et al., 2002). Langmuir et al., (1992), however, predicted a maximum of 20% melting possible beneath mid oceanic ridge, constrained by the disappearance of clinopyroxene. Mckenzie, (1984), on the other hand, provided an estimate of 24.5%. It has been shown that the melt fraction increases with decreasing pressure, by 1-2%/Kbar (Langmuir et al., 1992). Based on this dynamic constraint of decompression melting, the melt fraction goes up to 20%.

Seismological studies have been extensively used to estimate the amount of melting as well as to delineate melt-rich mushy zones beneath MORS. MELTS (Forsyth et al., 1998) observations in EPR suggest that although the total region of melt availability, as indicated by low seismic velocities, may cover a depth up to 180 km, extractable melts beneath the ridge occur up to a depth of 60 to 70 km. It is also observed that the low velocity zone can occur at a shallow depth (~15 km). The amount of melt here may not be well constrained, but the shapes of melt zones are well constrained. They occur as thin films or melt tubes/pockets (Eberle & Forsyth, 1998).

Another constraint of decompression melting relates to the thinness of MOR crust, which further complicates in modelling the ridge melting processes. Based on a limited number of seismic data sets for active spreading centres, (Behn & Grove, 2015) constrained the average crustal thickness of 6 to7 km when the half spreading rate is >10 mm/yr (FSR), and 2 to 4 km for spreading rates <10 mm/yr (SSR). Behn & Grove, (2015) showed from a 2D numerical model that a reduced contribution of the off-axis melt lowers the crustal thickness, more so when the mantle potential temperature is high. Furthermore, high spreading rates favour production of more off-axis melts, which are assumed to re-solidify with progressive cooling and crystallization in the overlying lithosphere. Consider a cut off distance of 25 km from the ridge, (Behn & Grove, 2015) estimated the crustal thickness decreasing by 30 to 40% to attain a thickness of 4 km for a half-spreading rate of 2-6 cm/yr and a mantle potential temperature of 1300^0C. However, had the mantle potential temperature been set at 1350^0C or more (e.g., 1400 and 1450^0C), the crustal thickness reduction would be double or triple, albeit the final thickness would remain above 5km, sometimes close to 10 km. Given such a large crustal thickness, the pooling area beneath first spreading ridges should be quite narrow. Moreover, in cases of slow

spreading ridges, the crustal thickness is expected to be less than 5 km and the pooling area would be narrowed accordingly.

S.3 Fluid-Structure Interaction: Theoretical formulation

The theoretical operations in handling FSI problems adopts one of the two basic approaches: *integrated* and *partitioned*. The present theoretical treatment follows the partition approach, which is computationally less expensive, and also saves both computation time as well as complexity (Hou et al., 2012). According to the classical mechanics, a fluid-structure interface should satisfy Dirichlet and Neumann transmission conditions (Fernández & Moubachir, 2005). The velocity transmission from solid to fluid in a FSI system is called Dirichlet boundary condition, whereas the normal stress transmission from fluid to solid is called Neumann boundary condition. We employed the Robin transmission condition, which accounts for a linear combination of the Dirichlet and Neumann transmission conditions (Nobile & Vergara, 2007), keeping in view that the fluid and solid media are of the same spatial dimension, but the solid domain is much thinner than the fluid domain, as applicable to our present problem. This specific geometrical consideration simplifies the modelling approach to a large extent, reducing it to a one-way FSI system (transmission of fluid attributes onto the structure at their interface accounted at each time-step, without a loop-back transmission from structure to fluid). This manipulation treats the problem with a one-way Robin-Robin transmission condition (Badia et al., 2008). A skeletal mathematical description is given below to show the governing equations for the FSI transmission condition. The Neumann boundary condition for the structure can be expressed as:

$$\rho_s \delta_{tt} \hat{w}^{k+1} - \nabla \hat{t}_s^{k+1} = \hat{f}_s \text{ in } \Omega_0^s \tag{s1}$$

$$\tau_s{}^{k+1}.n_s = -\tau_f{}^{k+1}.n_f \text{ on } \Sigma^t, \tag{s2}$$

where the subscripts s and f denote the solid domain and fluid domain respectively.

We use $f^{(n)}$ as an approximation for a time-dependent function f at time level $t^{(n)}$. Backward difference operator δ_t is defined as $\delta_t f^{(n+1)} = \left(f^{(n+1)} - f^{(n)}\right)/\Delta t$, and $\delta_{tt}(.) = \delta_t\left(\delta_t(.)\right)$. $\hat{w}$ denotes displacement in the solid medium with respect to the reference configuration. The superimposed hat symbol indicates the values sought. Superscript *k* stands for the current iteration; hence *k+1* represents the next iteration. n_f is the outward normal to Ω_t^f on Σ^t [fluid-structure interface] and $n_s = -n_f$. The solid medium is assumed to be elastic and follows the constitutive relation between Cauchy stress tensor τ_s and deformation gradient tensor $\nabla\hat{w}$: $F(\hat{w}) = I + \nabla\hat{w}$.

In the integrated approach, one employs an integrated solver in implementing the algorithm while solving both fluid and structure problem. This mathematical scheme strictly couples the transmission conditions between solid and fluid at each numerical iteration. But the FSI problems in reality involve non-linearity in the physical setting, e.g., geometrical non-linearity at the fluid-solid interface. Moreover, the fluid domain itself can develop nonlinearity due to various dynamical reasons, such the convective term in the momentum equation (Eq. 2), which would pose a serious hurdle in implementing an integrated algorithm. The partitioned approach, on the other hand, solves the dynamic equations (Eq. 7) for solid and fluid separately, however, enforcing the conditions of continuity of velocity and normal stresses at the interface, and coupling of the transmission conditions at each time-step.

The nominal Dirichlet term acts as a perturbation to the crustal base to localize short-wavelength undulations, whereas the Neumann boundary condition gives rise to first-order, long-wave vertical undulations, and localizes 3D deformations in the elastic crust. In order to obtain both long- and short-wavelength axial topography, we impose a linear combination of the two

types of interactions at the interface (Badia et al., 2008)). The Dirichlet terms utilize the velocity of fluid domain at interface, described by a 3D array with three velocity components on one dimension, 18750 spatial points on the second dimension and 111 temporal points (covering 7 Myr) on the third dimension. For the Neumann term, the normal component of a strain-rate tensor at the fluid-solid interface in Eq. 10 is obtained from the vertical component of the fluid velocity vector, corresponding to a two-dimensional array of spatiotemporal points, considering a very small slope (3^o) of the interface. Our estimate yields a strain-rate median of 10^{-5} s^{-1} at the axis, with upper and lower limits, 10^{-3} s^{-1} and 10^{-11} s^{-1} on the interface, depending on the vertical component of the velocity.

Implementation of this partition procedure in the present model has been carried out through a range of simplification and idealization. a) First, as the model has a thinner solid domain, it is assumed that the structural dynamics does not affect the fluid domain kinematics. In other words, this is a one-way FSI mechanical setting, where the fluid has been solved independently over a time frame of 7 Myr, and the velocity data of more than 100 time instances have been stored. b) Second, as the present CFD modelling considers an almost rigid fluid domain overlying crust, whose viscosity is greater than the underlying mantle mush by an order of six (Table 1). Under this condition the crust-mantle interface in the fluid model completely dampens the velocity. The velocity values of the next layer of cell nodes are averaged with those of the interface cell nodes, and stored them as the fluid velocity of FSI interface (Fig. 1). c) In the FSI implementation, the viscous stress part in equation 9 is a product of normal-to-surface component of strain rate and dynamic viscosity of the fluid. We use a dynamic viscosity of fluid for the Robin transmission condition different from that obtained from the CFD model. In a CFD model, a reference viscosity for mantle-mush is chosen in the order of 10^{15} Pa s, which decreases

further with rise in temperature following a power-law, where the variation is limited within one order. But, for the Robin transmission condition in FSI, the fluid viscosity that affects the interface is equated with that of top 10 km of the sub-crustal fluid domain. The effective viscosity of the magma-mush of top 10 km of the sub-crustal fluid domain has been estimated in the order of 10^{13} to 10^{15} Pa s (Sen et al., 2023). d) The normal-to-surface strain rate in describing the viscous stress part of Equation 9 has been idealized as the ratio of vertical component of the fluid velocity of the interface nodes and the thickness of the fluid domain of the CFD model, which represents the total height of the convection loop. e) The pressure part of Equation 9 has been idealized as a combination of normal dynamic pressure utilizing the vertical velocity component and a constant hydrostatic pressure. f) The essential part of the Robin transmission condition is the utilization of a scaled velocity component, as has been outlined in Equation 10. Numerical implementation of FSI is carried without this component (i.e., only Neumann), which produces a convex or concave crustal top surface each time without a narrow axial high or morphological complexity resembling MOR topography. But, implementation of the scaled velocity component (i.e., Robin transmission) in FSI gives rise to MOR topography. The scale factor has a positive and bounded value, which is set at 0.1. A trial with values ranging 2 to 0.005 has been carried out in order to ascertain the effect of it on the topography of the crustal top surface and the principal stresses. It is seen that the choice of scaling factor value has little effect in the range of 0.1 to 0.01, on both topography and principal stresses.

S.4 Vertical stress

We used the FSI model to estimate the vertical stress ($\sigma^{\uparrow}$), controlled by both the MOR topography and the underlying mush flow dynamics. The magnitude of $\sigma^{\uparrow}$ is found to largely vary from the top to the bottom crustal boundary, setting in a steep stress gradient with depth in

the crust. In the axial zones its median values for the top crustal layer show similar variations with time (Fig. S.1a) : tensile $\sigma^{\uparrow}$ = +10 MPa at 1 Myr and compressional $\sigma^{\uparrow}$ = -8.5 MPa at 1.5 Myr, dropping to: +6.7 MPa and -4 MPa at 2.5, and further to +4 MPa and -1.2 MPa at 7 Myr), respectively. The whole crustal layer produces remarkably higher vertical stress (+50 MPa and -60 MPa at 1 Myr, decreasing with time to +42 MPa and -32 MPa at 2.5 Myr and further to +23 MPa and -14 MPa at 7 Myr). The variation of vertical stress with depth is exceptionally strong, as evident from the stress ratio between the top and the bottom boundaries (7 at 1 Myr and 5.7 at 7 Myr for tensile stress, and 7 at 1-1.5 Myr and 12 at 7 Myr for compressive stress), implying that the elastic crust completely attenuates the vertical stress within crust (Fig. S.1b). The off-axis regions develop a peak of the median of vertical stresses peak at around 3 Myr and thereafter stabilizes $\sigma^{\uparrow}$. In the top crustal layer, the median of the off-axis stress field is lower (+3.1 MPa and -3.7 MPa at 3 Myr, dropping down to +1.7 MPa and -1 MPa at 7 Myr) than that in the axial zones (Fig. S.1 b). For the whole crustal layer, the stress medians show similar temporal variations (+7.8 MPa and -27 MPa at 4 Myr, decreasing to +4.8 MPa and -15 MPa at 7 Myr), and stress ratios between the top and the whole crustal layer (tensile $\sigma^{\uparrow}$: 2.5 at 3-4 Myr to 2.8 at 7 Myr, and compression $\sigma^{\uparrow}$: 7.3 at 4 Myr to 15 at 7 Myr) (Fig. S.1b).

The model shows several off-axis, deep-crustal regions with compressive vertical stresses significantly greater than the vertical tensile stress, which is evident from the high 75^{th} percentiles in boxplots (Fig. S.1a). The axial zones in the top crustal layer contain discrete high compressive zones corresponding to hill topography, which is replaced by high tensile stress concentrations in the bottom layer beneath the hills. There are some across-axis narrow zones of compressive stress fields, separated by broad low stress zones in both top and bottom layers of the crust (Fig. S.1a), which signify segment boundaries in the MOR setting.

S.5 Von-Mises stress calculations

According to shear-energy theory (Barsanescu & Comanici, 2017), the second invariant of a deviatoric stress tensor reaches a critical value before a ductile material starts yielding. That second invariant of the deviatoric stress of a material or von-Mises stress is expressed in terms of the three principal stresses as,

$$\sigma^{vm} = \{[(\sigma_1 - \sigma_2)^2 + (\sigma_2 - \sigma_3)^2 + (\sigma_1 - \sigma_3)^2] / 2\}^{1/2} \quad \text{(s3)}$$

The present model calculates the von-Mises stress of the crust, which is presented by 3D contouring in Fig. S.3a and S.3b exhibits box-plots of the von-Mises stresses at various sections. The stress medians at axial zones reach their peaks at 1 Myr (500 MPa at top-crustal layer and 680 MPa for whole crust) and attain steady state at 7 Myr (200 MPa at top-crustal layer and 220 MPa in case of whole crust). On the other hand, von-Mises stress medians at off-axis zones peak at 3 Myr (80 MPa for top-crustal layer and 125 MPa for whole crust) and decrease nominally (75 MPa for top-crustal layer and 109 MPa for whole crust) in course of time. Overall, von-Misses stress contours suggest that axial zones failures could be generated by magmatic activity alone while off-axis failures could be triggered by magmatic activity but associated plate movements may be needed to engender a fault. It could also be inferred that cumulative shear is responsible for ridge-transverse orthogonal lengthy failures, as high von-Misses stress strips are visible off-axis (Fig. S.3a).

References

Badia, S., Nobile, F., & Vergara, C. (2008). Fluid-structure partitioned procedures based on Robin transmission conditions. *Journal of Computational Physics*, *227*(14). https://doi.org/10.1016/j.jcp.2008.04.006

Barsanescu, P. D., & Comanici, A. M. (2017). von Mises hypothesis revised. *Acta Mechanica*, *228*(2). https://doi.org/10.1007/s00707-016-1706-2

Behn, M. D., & Grove, T. L. (2015). Melting systematics in mid-ocean ridge basalts: Application of a plagioclase-spinel melting model to global variations in major element chemistry and crustal thickness. *Journal of Geophysical Research: Solid Earth*, *120*(7). https://doi.org/10.1002/2015JB011885

Eberle, M. A., & Forsyth, D. W. (1998). An alternative, dynamic model of the axial topographic high at fast spreading ridges. *Journal of Geophysical Research: Solid Earth*, *103*(6). https://doi.org/10.1029/98jb00437

Edmonds, M., Cashman, K. V., Holness, M., & Jackson, M. (2019). Architecture and dynamics of magma reservoirs. In *Philosophical Transactions of the Royal Society A: Mathematical, Physical and Engineering Sciences* (Vol. 377, Issue 2139). https://doi.org/10.1098/rsta.2018.0298

Fernández, M. A., & Moubachir, M. (2005). A Newton method using exact jacobians for solving fluid-structure coupling. *Computers and Structures*, *83*(2–3). https://doi.org/10.1016/j.compstruc.2004.04.021

Forsyth, D. W., Scheirer, D. S., Webb, S. C., Dorman, L. M., Orcutt, J. A., Harding, A. J., Blackman, D. K., Phipps Morgan, J., Detrick, R. S., Shen, Y., Wolfe, C. J., Canales, J. P., Toomey, D. R., Sheehan, A. F., Solomon, S. C., & Wilcock, W. S. D. (1998). Imaging the deep seismic structure beneath a mid-ocean ridge: The MELT experiment: The MELT seismic team. *Science*, *280*(5367). https://doi.org/10.1126/science.280.5367.1215

Hou, G., Wang, J., & Layton, A. (2012). Numerical methods for fluid-structure interaction - A review. In *Communications in Computational Physics* (Vol. 12, Issue 2). https://doi.org/10.4208/cicp.291210.290411s

Johan Lissenberg, C., MacLeod, C. J., & Bennett, E. N. (2019). Consequences of a crystal mush-dominated magma plumbing system: A mid-ocean ridge perspective. *Philosophical Transactions of the Royal Society A: Mathematical, Physical and Engineering Sciences*, *377*(2139). https://doi.org/10.1098/rsta.2018.0014

Langmuir, C. H., Klein, E. M., & Plank, T. (1992). Petrological systematics of mid-ocean ridge basalts: Constraints on melt generation beneath ocean ridges BT - … melt generation at mid-ocean …. In *... melt generation at mid-ocean ...* (Vol. 71).

Langmuir, C. H., Klein, E. M., & Plank, T. (2013). *Petrological Systematics of Mid-Ocean Ridge Basalts: Constraints on Melt Generation Beneath Ocean Ridges*. https://doi.org/10.1029/gm071p0183

Mckenzie, D. (1984). The generation and compaction of partially molten rock. *Journal of Petrology*, *25*(3). https://doi.org/10.1093/petrology/25.3.713

Mckenzie, D., & Bickle, M. J. (1988). The volume and composition of melt generated by extension of the lithosphere. *Journal of Petrology*, *29*(3). https://doi.org/10.1093/petrology/29.3.625

Nobile, F., & Vergara, C. (2007). An effective fluid-structure interaction formulation for vascular dynamics by generalized Robin conditions. *SIAM Journal on Scientific Computing*, *30*(2). https://doi.org/10.1137/060678439

Presnall, D. C., Gudfinnsson, G. H., & Walter, M. J. (2002). Generation of mid-ocean ridge basalts at pressures from 1 to 7 GPa. *Geochimica et Cosmochimica Acta*, *66*(12). https://doi.org/10.1016/S0016-7037(02)00890-6

Sen, J., Sarkar, S., & Mandal, N. (2023). Control of mush complex viscosity on mid-ocean ridge topography: A fluid–structure model analysis. *Physics of Fluids*, *35*(6). https://doi.org/10.1063/5.0152667

Singh, S. C., Crawford, W. C., Carton, H., Seher, T., Combier, V., Cannat, M., Canales, J. P., Düsünür, D., Escartin, J., & Miranda, J. M. (2006). Discovery of a magma chamber and faults beneath a Mid-Atlantic Ridge hydrothermal field. *Nature*, *442*(7106). https://doi.org/10.1038/nature05105

Singh, S. C., Kent, G. M., Collier, J. S., Harding, A. J., & Orcutt, J. A. (1998). Melt to mush variations in crustal magma properties along the ridge crest at the southern East Pacific Rise. *Nature*, *394*(6696). https://doi.org/10.1038/29740

Sinton, J. M., & Detrick, R. S. (1992). Mid-ocean ridge magma chambers. *Journal of Geophysical Research*, *97*(B1). https://doi.org/10.1029/91JB02508

Sparks, R. S. J., Annen, C., Blundy, J. D., Cashman, K. V., Rust, A. C., & Jackson, M. D. (2019). Formation and dynamics of magma reservoirs. In *Philosophical Transactions of the Royal Society A: Mathematical, Physical and Engineering Sciences* (Vol. 377, Issue 2139). https://doi.org/10.1098/rsta.2018.0019

Figure S.1

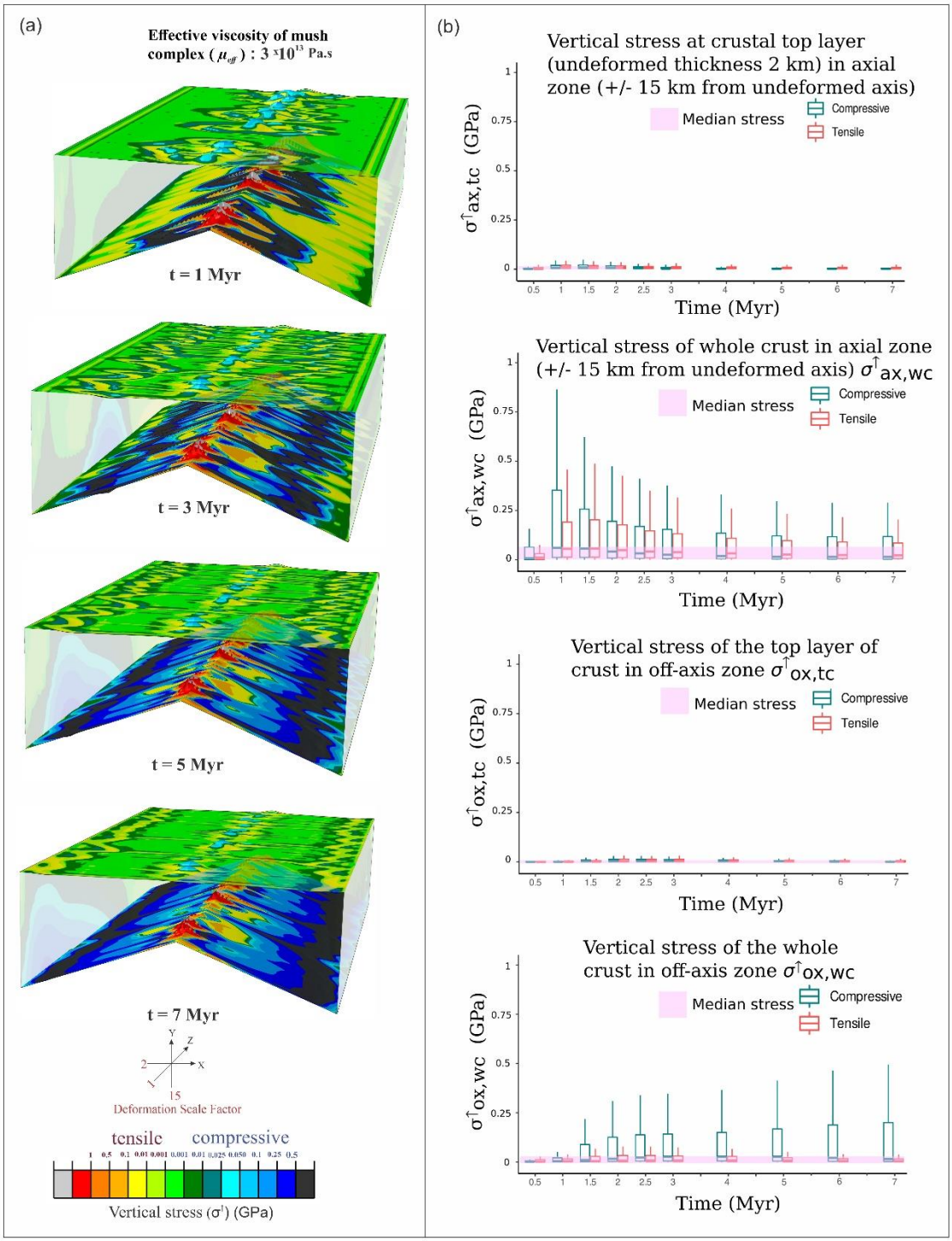
(a)
Effective viscosity of mush complex (μ_{eff}) : 3×10^{13} Pa.s
t = 1 Myr
t = 3 Myr
t = 5 Myr
t = 7 Myr
Deformation Scale Factor
tensile
compressive
Vertical stress ($\sigma^{\uparrow}$) (GPa)
(b)
Vertical stress at crustal top layer (undeformed thickness 2 km) in axial zone (+/- 15 km from undeformed axis)
Median stress
Compressive
Tensile
$\sigma^{\uparrow}_{ax,tc}$ (GPa)
Time (Myr)
Vertical stress of whole crust in axial zone (+/- 15 km from undeformed axis) $\sigma^{\uparrow}_{ax,wc}$
$\sigma^{\uparrow}_{ax,wc}$ (GPa)
Vertical stress of the top layer of crust in off-axis zone $\sigma^{\uparrow}_{ox,tc}$
$\sigma^{\uparrow}_{ox,tc}$ (GPa)
Vertical stress of the whole crust in off-axis zone $\sigma^{\uparrow}_{ox,wc}$
$\sigma^{\uparrow}_{ox,wc}$ (GPa)

Figure S.1

A time series 3D analysis of the vertical stress and their statistical box-plots for different zones in Mid-Oceanic ridge. a) Vertical stress ($\sigma^{\uparrow}$) contour (σ_{yy} in Cartesian model setting) plots from model runs at 1, 3, 5, and 7 Myr model run time (Model scales: vertical = 15, along-axis = 1, across-axis = 2) and transparent model views for visualization of the stress fields in both top and bottom layers. b) Statistical box-plots of stresses in the axial zone, off-axis zone, top-crustal layer, and whole-crust, showing their medians and quartiles.

Figure S.2

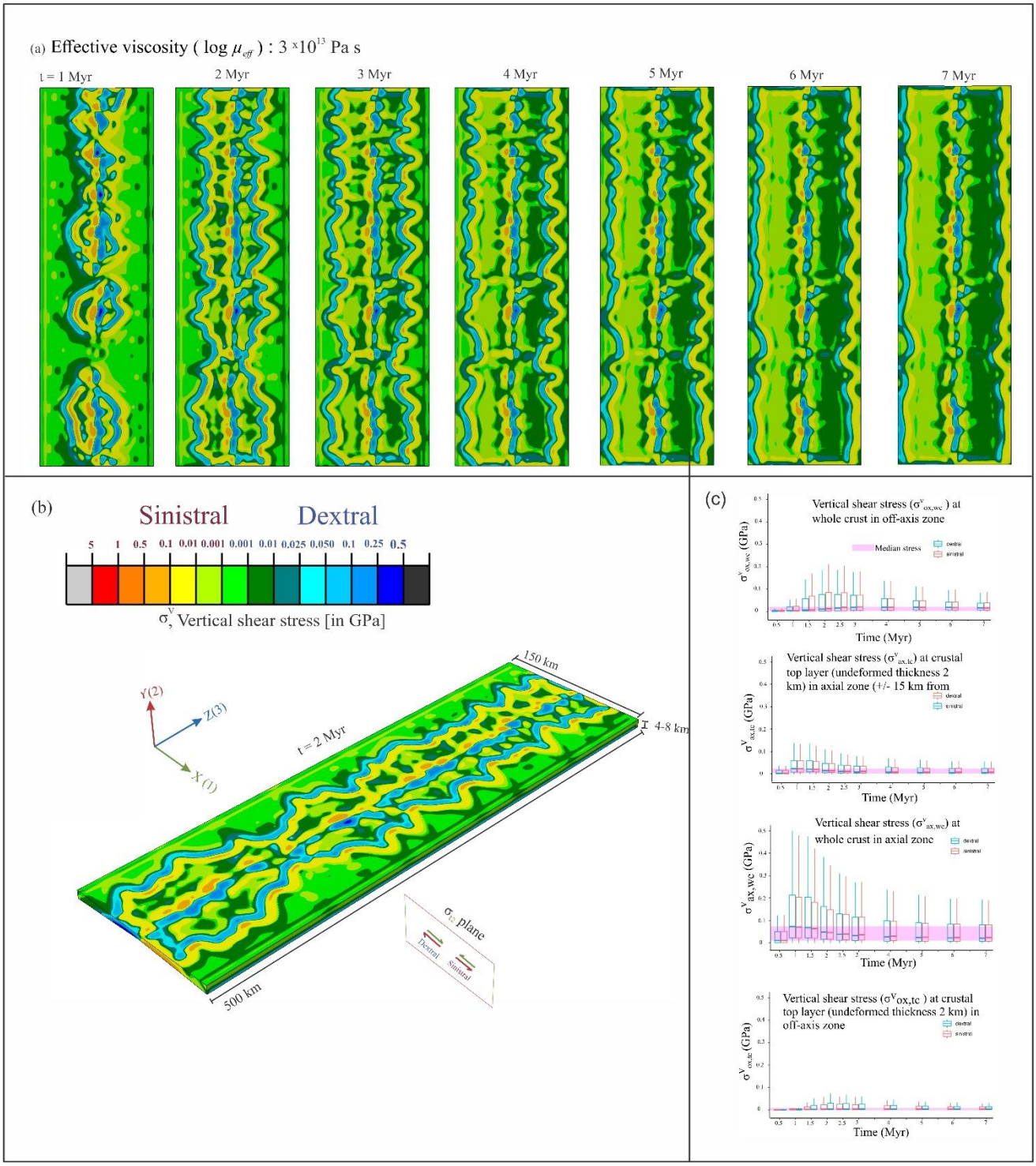
(a) Effective viscosity (log μ_{eff}) : 3 x10^{13} Pa s
t = 1 Myr
2 Myr
3 Myr
4 Myr
5 Myr
6 Myr
7 Myr
(b)
Sinistral
Dextral
5 1 0.5 0.1 0.01 0.001 0.001 0.01 0.025 0.050 0.1 0.25 0.5
σ^{v}, Vertical shear stress [in GPa]
Y(2)
Z(3)
X(1)
t = 2 Myr
150 km
4-8 km
500 km
σ$_{yz}$ plane
Dextral
Sinistral
(c)
Vertical shear stress (σ$^{v}_{ox,wc}$) at whole crust in off-axis zone
Median stress
dextral
sinistral
σ$^{v}_{ox,wc}$ (GPa)
Time (Myr)
Vertical shear stress (σ$^{v}_{ax,tc}$) at crustal top layer (undeformed thickness 2 km) in axial zone (+/- 15 km from
σ$^{v}_{ax,tc}$ (GPa)
Time (Myr)
Vertical shear stress (σ$^{v}_{ax,wc}$) at whole crust in axial zone
σ$^{v}_{ax,wc}$ (GPa)
Time (Myr)
Vertical shear stress (σ$^{v}_{ox,tc}$) at crustal top layer (undeformed thickness 2 km) in off-axis zone
σ$^{v}_{ox,tc}$ (GPa)
Time (Myr)

Figure S.2

Contour plots of the vertical shear stresses and the box-plots of the stresses in MOR. a) Vertical shear stress contours (σ_{xy} in Cartesian model settings) obtained from model runs at 1, 2, 3, 4, 5, 6, and 7 Myr, with counterclockwise (sinistral) and clockwise (dextral) mapping to depict the dynamic evolution of vertical shear in the crust. b) A contour plot in the three-dimensional model view at 2 Myr, showing sinistral and dextral vertical shear in a Cartesian model frame. c) Corresponding statistical box-plots with the median stress values and their quartiles.

Figure S.3

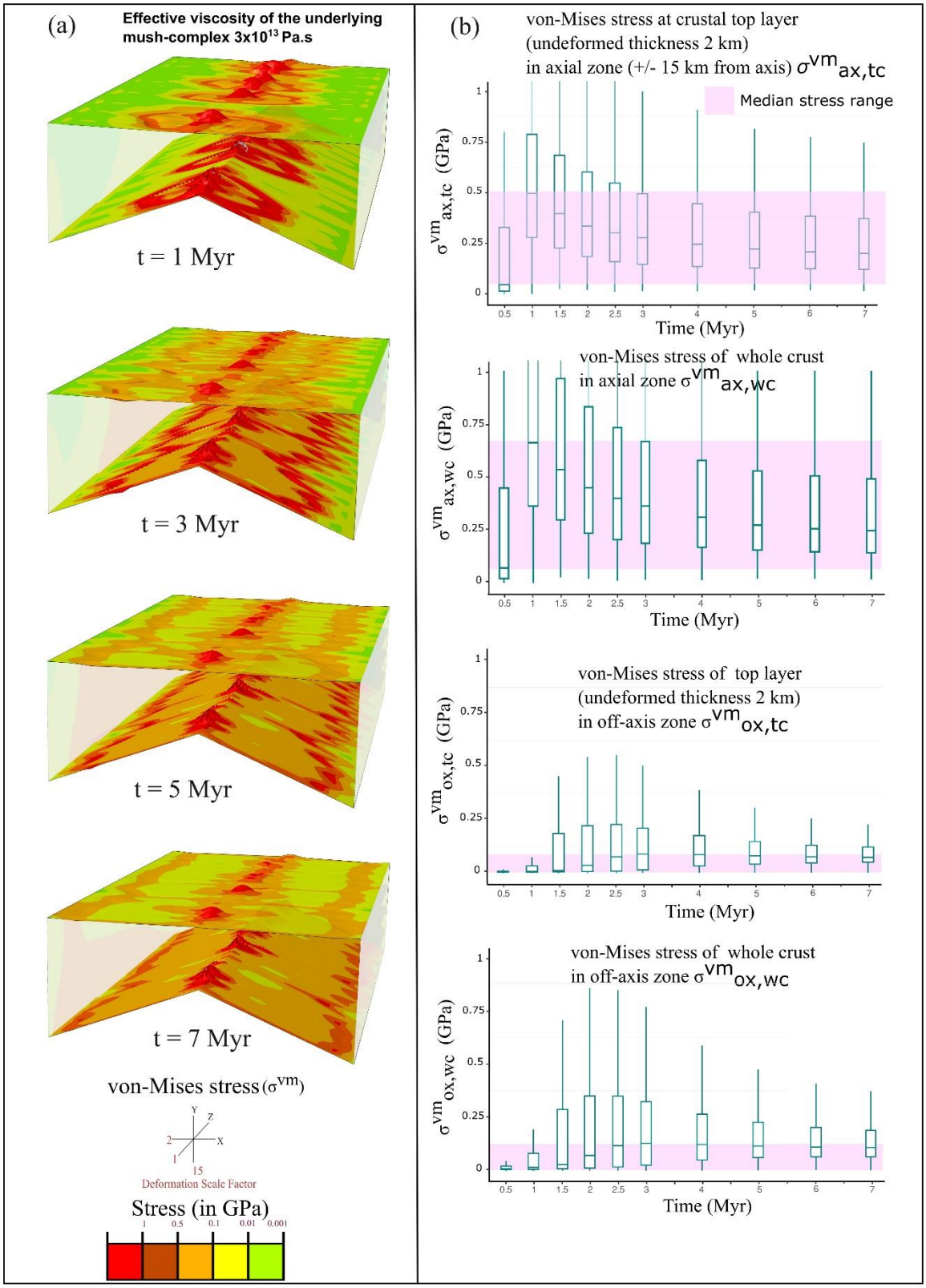
(a)
Effective viscosity of the underlying mush-complex 3x10^13 Pa.s
t = 1 Myr
t = 3 Myr
t = 5 Myr
t = 7 Myr
von-Mises stress (σ^vm)
Deformation Scale Factor
Stress (in GPa)
1
0.5
0.1
0.01
0.001
(b)
von-Mises stress at crustal top layer
(undeformed thickness 2 km)
in axial zone (+/- 15 km from axis) σ^vm ax,tc
Median stress range
σ^vm ax,tc (GPa)
Time (Myr)
von-Mises stress of whole crust
in axial zone σ^vm ax,wc
σ^vm ax,wc (GPa)
Time (Myr)
von-Mises stress of top layer
(undeformed thickness 2 km)
in off-axis zone σ^vm ox,tc
σ^vm ox,tc (GPa)
Time (Myr)
von-Mises stress of whole crust
in off-axis zone σ^vm ox,wc
σ^vm ox,wc (GPa)
Time (Myr)

Figure S.3

A time series 3D contour plots for von-Misses stress and their statistical box-plots for different model MOR regimes. a) von-Misses stress (σ^{vm}) contours for 1, 3, 5, and 7 Myr (Model scales: vertical = 15, along-axis = 1, across-axis = 2) and corresponding transparent representation, showing the stress fields in both the top and bottom layers. b) Statistical box-plots of stresses in the axial zone, off-axis zone, top-crustal layer, and whole-crust, along with their medians and quartiles.

Figure S.4

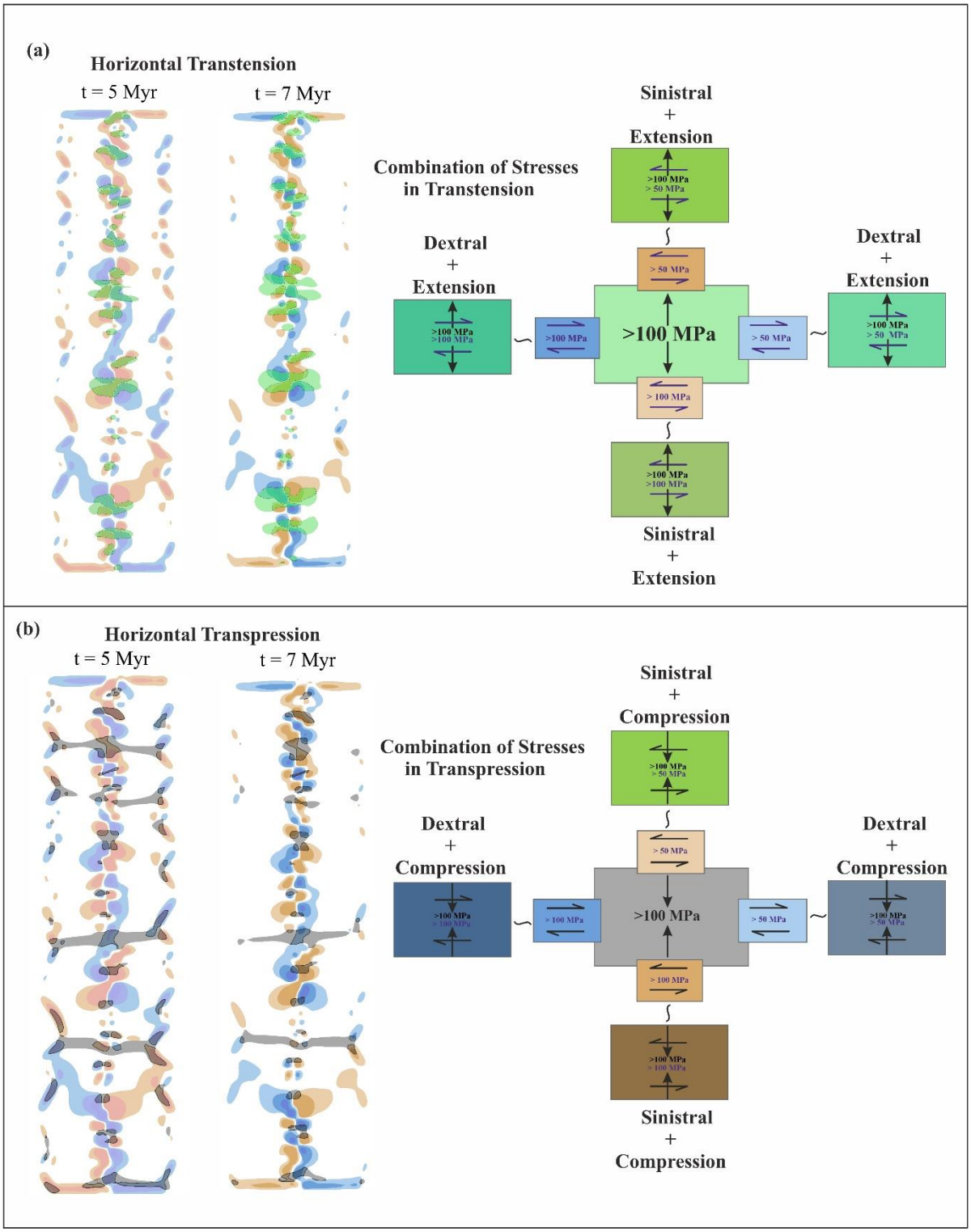
(a)
Horizontal Transtension
t = 5 Myr
t = 7 Myr
Combination of Stresses in Transtension
Sinistral + Extension
Dextral + Extension
Dextral + Extension
Sinistral + Extension
>100 MPa
(b)
Horizontal Transpression
t = 5 Myr
t = 7 Myr
Combination of Stresses in Transpression
Sinistral + Compression
Dextral + Compression
Dextral + Compression
Sinistral + Compression
>100 MPa

Figure S.4
a) Vertical and Horizontal transtensional stress fields. Areas enclosed by black outlines denote the transtensional zone. A cartoon diagram is also provided to show sinistral and dextral shears along with the axis-parallel tension. b) Similar contour presentation for axis-parallel compression.